

Modelling ice island calving events with Finite Element Analysis

by

Jesse Smith

A thesis submitted to the Faculty of Graduate and Postdoctoral
Affairs in partial fulfillment of the requirements for the degree of

Master of Science

in

Geography with a Specialization in Data Science

Carleton University
Ottawa, Ontario

© 2020
Jesse Smith

Abstract

Ice islands, massive tabular icebergs, are known to fracture (calve) into fragments as they drift. One proposed calving mechanism occurs when a large protuberance, known as a ram, develops along the submerged edge of the ice island and induces a bending stress due to its buoyancy. To examine the relationship between rams and ice island fracture, polygons of ice islands derived from remote sensing imagery were used to create 3-D representations with synthesized rams. Associated stress and fractures were predicted using a Finite Element Analysis (FEA) and the results were compared to polygons of the actual fractured pieces. Modelled ice islands calve accurately when a synthesized ram is placed only along the edge that breaks off. An empirical model was developed to predict stress magnitude, which indicated the length of the ram, ram extent, and the ratio of ram volume to total ice volume play a central role in calving.

Acknowledgments

I am exceedingly thankful to Derek Mueller for taking me on as a student and encouraging me to embrace quantitative research and computer programming, for giving me the chance to conduct fieldwork in the Arctic, and for the excellent quality of feedback and guidance throughout my time as a graduate student at the Water and Ice Research Laboratory (WIRL) at Carleton University.

My co-supervisor, Gregory Crocker, and Mahmud Sazidy were also necessary for the completion of this thesis. I am grateful for their recommendations and support on the technically-challenging aspects of my project. The staff at LS-DYNA have been wonderfully patient with my never-ending questions about the software, and Abass Braimah provided access to the software. My fellow lab mates at WIRL provided a lot of assistance with general GIS, statistics, and Microsoft Word problems whenever the Internet (or my short attention span) failed me.

My fieldwork would not have gone smoothly without the assistance of Adam Garbo, Abigail Dalton, Claire Bernard Grand-Maison, Guillaume Carpentier, Jade Brossard, and all of the crew aboard the *CCGS Amundsen* during Leg 3 of the summer 2018 science cruise. I'm still in awe that we managed to get the data in spite of many setbacks.

My research was made possible from funding from: the Early Career Researcher Award (Ontario Ministry of Research and Innovation), ArcticNet, Northern Scientific Training Program (NSTP), Amundsen Science, and the Ina Hutchison Award in Geography.

Lastly, I would like to express my gratitude to my mother, Nicole, for her continued emotional support and driving me around Ontario when I was trying to pick a graduate program two years ago (no regrets), my dad, Richard, for bringing me back and forth

from Ottawa to Sudbury countless times, my friends for being generally "rad" (too many to thank individually), Caitlin for showing interest and putting up with my server-related meltdowns, the staff at Bar Robo for all the coffee and karaoke, and finally, my band Stoby for getting my mind off of giant tabular icebergs on weekends.

Table of contents

Abstract.....	ii
Acknowledgments	iii
Table of contents	v
List of figures	vii
List of tables	ix
1.0 Introduction.....	1
1.1 Research objectives	4
1.2 Structure of this thesis.....	5
2.0 Literature review.....	6
2.1 Ice island morphology	6
2.2 Ice island drift.....	10
2.3 Ice island deterioration.....	12
2.4 Buoyancy of ice islands.....	19
2.5 The ‘footloose’ mechanism.....	20
2.6 Previous calving models	22
2.7 Finite Element Analysis.....	24
3.0 Methods	28
3.1 Ice island nominal thickness estimation.....	28
3.2 Ice island selection	29
3.3 Meshing and ram creation	31
3.4 Material properties, forces, and simulation settings	33
3.4.1 Segment set and height of the waterline	34
3.4.2 Damping coefficients	34
3.5 Compiling solutions	37
3.6 Sensitivity analysis.....	38
3.7 Ram orientation analysis.....	38
3.8 Reduced localized ram extent analysis.....	41
3.9 Limitless flexural strength analysis.....	41
3.10 Empirical modelling	42
4.0 Results	44
4.1 Ice island nominal thickness estimation results.....	44
4.2 Sensitivity analysis results.....	47
4.3 Uniform ram results	49

4.4 Localized ram results	50
4.5 Reduced localized ram extent results.....	52
4.6 Limitless flexural strength results.....	54
4.7 Empirical model results	56
5.0 Discussion	60
5.1 Ram morphology	60
5.1.1 Symmetrical rams	60
5.1.2 Localized rams	62
5.1.3 Effect of a reduced ram extent	63
5.2 Variations in flexural strength.....	64
5.3 Ice rheology	65
5.4 Statistical model parameters.....	65
5.5 Model limitations.....	67
5.6 Future work.....	69
6.0 Conclusion	72
7.0 References.....	77
8.0 Appendix A.....	88
8.1 Simulation video of an ice island mesh 1 – uniform	88
9.0 Appendix B.....	89
9.1 Simulation video of an ice island mesh 2 – localized	89
10.0 Appendix C.....	90
10.1 Simulation video of an ice island mesh 3 – localized, shortened	90

List of figures

FIGURE 2.1: PHOTOGRAPH OF AN ICE ISLAND ("PII-A-1-F") GROUNDED AT 67° 21.4' N, 63° 15.2'W, APPROXIMATELY 40 KM TO THE SOUTHEAST OF QIKIQTARJUAQ, NU.	7
FIGURE 2.2: DIAGRAM OF AN ICE ISLAND.	7
FIGURE 2.3: CALVING EVENT AT PETERMANN GLACIER (NORTHWEST GREENLAND) IMAGED ON 17 AUGUST, 2010 BY LANDSAT 7.	9
FIGURE 2.4: GENERALIZED DRIFT TRAJECTORIES OF EASTERN CANADIAN ICE ISLANDS (A), AND WESTERN CANADIAN ICE ISLANDS (B).	10
FIGURE 2.5: TRAJECTORIES OF VARIOUS ICE ISLANDS AND ICEBERGS OVERLAPPING SHIP TRAFFIC DENSITY (GREYSCALE LEGEND) AND OIL AND GAS EXPLORATION LEASES (RED).	12
FIGURE 2.6: PROFILE VIEW OF ICE ISLAND DETERIORATION PROCESSES.	13
FIGURE 2.7: MULTIPLE OVERLAID RADARAT-2 DIGITIZATIONS OF ICE ISLAND "PII-A-1-F" BETWEEN 2015-2017, SHOWING ITS CHANGE IN POSITION AND ASSUMED ROTATION.	15
FIGURE 2.8: STRESS AND STRAIN CURVES SHOWING THE DIFFERENT POSSIBLE DEFORMATION CHARACTERISTICS OF AN UNSPECIFIED MATERIAL (1) AND FOR ICE UNDER INCREASING RATES OF APPLIED STRESS (2).	16
FIGURE 2.9: DIAGRAM OF POISSON’S RATIO OF A 2-D CYLINDER.	19
FIGURE 2.10: DIAGRAM OF THE ‘FOOTLOOSE MECHANISM’	21
FIGURE 2.11: A SIMPLE 2-D RECTANGULAR DOMAIN (A) AND ITS MESH DIVIDED INTO 4 ELEMENTS WHOSE EXTENTS ARE DELINEATED BY 4 NODES EACH (B).	25
FIGURE 2.12: TYPES OF 3-D ELEMENTS; 3-D TETRAHEDRON (A & B) AND HEXAHEDRON (C) ELEMENTS ARE EACH SHOWN WITH LINEAR SHAPE FUNCTIONS.	26
FIGURE 3.1: SAMPLE ‘CALVING PLOT’ OF INSTANCE “20101106_113811_r2_12_LWT”.	30
FIGURE 3.2: PROFILE VIEW OF A SAMPLE ICE ISLAND MESH.	32
FIGURE 3.3: THE POLYGON TO 3-D ICE ISLAND MESH PROCESS.	32
FIGURE 3.4: MANUAL DETERMINATION OF DAMPING COEFFICIENTS.	36
FIGURE 3.5: EQUATION TO AUTOMATICALLY DETERMINE DAMPING COEFFICIENTS.	37
FIGURE 3.6: CREATION OF A LOCALIZED RAM ON ICE ISLAND “20120911_115220_r2_1_IKY”.	40
FIGURE 3.7: EXAMPLE OF AN ICE ISLAND MESH ("20110705_214859_r1_0_BSS") WITH A RAM LENGTH OF 60 M LOCALIZED TO THE CALVING EDGE (C).	40
FIGURE 4.1: TRANSECT RESULTS OF ICE ISLAND "PII-A-1-F".	44
FIGURE 4.2: DISTRIBUTION OF THE MODELLED ICE ISLANDS.	46

FIGURE 4.3: NETWORK GRAPH OF THE MODELLED ICE ISLANDS REPRESENTED BY NODES (CIRCLES) AND SUBSEQUENTLY CALVED FRAGMENTS (DAUGHTERS) IN MATCHING COLOURS.	47
FIGURE 4.4: TIME STEP HISTORY OF THE ELEMENT WHICH REACHES THE MAXIMUM OF MPS AT EACH STATE PLOTTED FOR 4 DIFFERENT MESH RESOLUTIONS.	49
FIGURE 4.5: COMPARISON BETWEEN A CALVING PLOT AND FEA SIMULATION RESULTS OF THE SAME ICE ISLAND.	50
FIGURE 4.6: ICE ISLAND SIMULATION SHOWING FAILURE FOR THE TOPMOST ELEMENT LAYER TO ERODE AFTER THE PROPAGATION OF A FRACTURE (RED BOX).	52
FIGURE 4.7: VARIOUS PLOTS OF MPS FROM THE LIMITLESS FLEXURAL STRENGTH ANALYSIS AS A FUNCTION OF DIFFERENT ICE ISLAND ATTRIBUTES (RAM LENGTH (A), SURFACE AREA (B), RAM EXTENT (C), AND RAM VOLUME (D)).	55
FIGURE 4.8: A SCATTERPLOT MATRIX OF THE TRANSFORMED VARIABLES INDICATING MODERATE RELATIONSHIPS BETWEEN MPS AND EACH OF RAM LENGTH AND RAM VOLUME.	56
FIGURE 4.9: THE MAXIMUM OF MPS OF EACH ICE ISLAND WITH A REGRESSION LINE PLOTTED THROUGH EACH SEPARATE NOMINAL CATEGORY OF TOTAL ICE VOLUME (LOW AND HIGH TOTAL VOLUME).	59
FIGURE 5.1: FRACTURE PATTERNS ON THE BOTTOM SURFACE OF ICE ISLAND "20101203_115225_r2_4_PJJ".	61
FIGURE 5.2: REGIME OF ICE ISLAND THICKNESS (H, X-AXIS) AND RAM LENGTH (L, Y-AXIS) AND WHETHER OR NOT A CALVING OCCURS (BREAKING/NO BREAKING).	64
FIGURE 5.3: SCHEMATIC OF AN ICE ISLAND TORQUEING (A) VERSUS TILTING (B).	67
FIGURE 5.4: POLYGONS OF ICE ISLAND INSTANCES "20101106_113811_r2_12_LWI" AND "20100805_160926_es_2_PYO" SHADED ACCORDING TO THEIR PREDICTED ABSOLUTE MPS WHEN OUTFITTED WITH A RAM LENGTH OF 20 M.	71
FIGURE 8.1: A CALVING PLOT AND THE SIMULATION RESULTS FROM AN ICE ISLAND ("20110705_214859_r1_0_BSS") WITH A 40 M LONG UNIFORM RAM.	88
FIGURE 9.1: A CALVING PLOT AND THE SIMULATION RESULTS FROM AN ICE ISLAND ("20110705_214859_r1_0_BSS") WITH A 40 M LONG LOCALIZED RAM.	89
FIGURE 10.1: A CALVING PLOT AND THE SIMULATION RESULTS FROM AN ICE ISLAND ("20110705_214859_r1_0_BSS") WITH A 40 M LONG LOCALIZED RAM WITH ITS EXTENT REDUCED BY HALF.	90

List of tables

TABLE 2.1: PARAMETER VALUES FOR THE ICE ISLAND CALVING FEA DEVELOPED BY SAZIDY ET AL. (2019).	24
TABLE 3.1: PARAMETERS FOR THE FEA ICE ISLAND MODEL	33
TABLE 4.1: ICE ISLANDS USED FOR FRACTURE MODELLING WITH THEIR PRE-FRACTURE SURFACE AREA, PERIMETER, LENGTH, AND THE PERCENTAGE OF MOTHER ICE ISLAND SURFACE AREA OCCUPIED BY THE DAUGHTERS.	45
TABLE 4.2: SENSITIVITY ANALYSIS RESULTS.	48
TABLE 4.3: VOLUME AND LENGTHS OF ICE ISLAND AND MESHES WITH RAM EXTENTS OF HALF THE ORIGINAL LOCALIZED EXTENT, WITH RAM VOLUME AS A PERCENTAGE OF TOTAL VOLUME.	53
TABLE 4.4: RESULTS OF THE MAXIMUM MPS OF THE FIVE ICE ISLANDS WITH A LOCALIZED RAM LENGTH OF 20 M WHEN ITS EXTENT WAS SHORTENED BY HALF THE ORIGINAL EXTENT.	54
TABLE 4.5: SKEWNESS BEFORE AND AFTER TRANSFORMATION OF ICE ISLAND VARIABLES	56
TABLE 4.6: SUMMARY TABLE OF THE MULTIPLE REGRESSION MODEL AND THE PERCENT OF TOTAL VARIATION EXPLAINED BY THE MODEL.	57
TABLE 4.7: ANCOVA SUMMARY TABLE. RAM LENGTH AND RAM EXTENT WERE STATISTICALLY SIGNIFICANT, SIMILAR TO THE MLR MODEL.	58
TABLE 4.8: LINEAR MODEL SUMMARY TABLE FOR THE ANCOVA MODEL COEFFICIENTS.....	59

1.0 Introduction

Climate change has had a particularly dramatic impact on the Canadian Arctic region, which is warming at three times the global average (Environment and Climate Change Canada, 2019). The rapid increase in temperatures has resulted in many changes to cryospheric features such as ice shelves and floating ice tongues, which now calve more frequently than in previous decades (Bevis et al., 2019; Rignot et al., 2011). Calving (detachment) of the termini of ice shelves and floating ice tongues gives way to massive tabular icebergs called ice islands (Benn et al., 2017). Calving events along the northern coast of Ellesmere Island, Canada's only remaining ice shelves, used to occur approximately once per decade (Jeffries and Sackinger, 1990) but, between 2000 to 2010, five major calving events were observed (Mueller et al., 2017). The reduction of Multi-year Land Fast Sea Ice (MLSI), a protective barrier to the ice shelves fringing northern Ellesmere Island (Mueller et al., 2003; Copland et al., 2007), and open water at the ice interface are thought to play a role in accelerating calving activity (Copland et al. 2017; Reeh et al. 2001). Increases in calving frequency have also occurred in Western Greenland's floating glacier tongues (Bevis et al., 2019), which discharge ice islands into the Eastern Canadian Arctic (Bigg et al., 2014), with Petermann Glacier calving over 430 km² between 2008 and 2012 (Crawford et al., 2018b).

It is expected that major calving events will continue to increase in the coming years and boost the production of ice islands (Bigg et al., 2014; Derksen et al., 2012) which are considered a potential risk for offshore infrastructure and shipping vessels (Bailey and Phillips, 2018; Eik and Gudmestad, 2010). Though many ice islands remain adrift or grounded in the Arctic Ocean, a considerable number of fragments drift as far south as

the Grand Banks region of Newfoundland where oil-drilling platforms are located (Flynn, 2013). As the Arctic warms, extensive reductions in sea ice during summers (Overland and Wang, 2013; Stroeve et al., 2008) are likely to spark interest in new offshore oil engineering projects at higher latitudes where ice islands are more abundant (Fuglem and Jordaan, 2017). Further, the shipping industry is poised to take advantage of shorter trans-oceanic routes through the Northwest Passage or directly across the Arctic Basin where these glacial hazards also exist (Smith and Stephenson, 2013).

The risk of collision between ice hazards and vessels needs to be considered in the context of these environmental changes (Dawson et al., 2018; Pizzolato et al., 2014). Historically, accidents are not unprecedented: The Ship Collision with Iceberg Database contains over 670 records of incidents over the last two centuries (Hill, 2010). In March of 2017 ~350 km southeast of Newfoundland, an iceberg drifted within 180 m of the *SeaRose* oil extraction platform (FPSO) (O'Neill-Yates, 2018). Operators of the *SeaRose* had knowledge of the incoming hazard but protocol to avoid a collision was not taken (CBC News, 2018). Ultimately, no accident took place, but the lack of action led to suspension of the *SeaRose* for a year (CBC News, 2018), bringing attention to the seriousness of ice hazard risk management and regulation. However, meaningful change requires a deeper understanding of iceberg drift mechanisms in order to inform risk interpretation within these policies.

Deterioration plays an important complementary role in risk forecasting. Ice islands sporadically calve smaller fragments that can be difficult to detect, but are still considered large enough to be a hazard to offshore activities (Van Wychen and Copland, 2017).

Sizes of calved fragments range from very large ice islands fragments, to icebergs, bergy

bits, and growlers (Canadian Ice Service, 2005). While much is understood about how ice islands deteriorate mass on smaller scales (thinning and so-called ‘edge-wasting’ events) (Crawford 2013), calving mechanisms are poorly understood and difficult to study (Wagner et al., 2014). Filling this knowledge gap would improve operational deterioration models and, coupled with drift models, improve understanding of how these ice hazards are created and distributed.

Diemand (1987), Scambos (2005), Wagner et al. (2014) identified a calving mechanism (dubbed “the footloose mechanism” by Wagner et al. (2014)) that describes how the development of an underwater ‘ram’ (an ice protrusion) along the submerged edge of the ice island induces a bending stress due to its buoyancy. When the resultant bending stress exceeds the flexural strength of the ice, a fracture propagates upwards resulting in a calving event. Finite Element Analysis (FEA, also sometimes referred to as the Finite Element Method (FEM)) can analyze stress distributions in all 3 dimensions (Fagan, 1992) which is ignored in previous 2-D calving models. Recently, an FEA model was developed by Sazidy et al. (2019) to test the effect of rams on icebergs. This new model can be used to evaluate the influence of different ram configurations on calving events. The recently released Canadian Ice Island Drift, Deterioration, and Detection database (CI2D3) has catalogued calving events and observations of drifting ice islands in the Eastern Arctic Ocean between 2008 and 2013 (Crawford et al., 2018b). The database, containing thousands of records (Crawford et al., 2018b), can query ice island calving events and presents an excellent opportunity to evaluate the influence of ram size and shape on real ice island calving events.

1.1 Research objectives

This thesis attempted to "reverse engineer" (technically a back analysis as ice islands are natural phenomena) the aftermath of calving events that were observed in remote sensing imagery by modelling the corresponding ice island shapes (prior to calving) with different ram dimensions. In order to accomplish this aim, Arctic fieldwork and descriptive data analysis was conducted and FEA modelling was performed using 3-D representations of ice island polygons with synthesized rams of various sizes. The objectives of the thesis were to:

1. Measure ice island morphological characteristics *in situ* to inform modelling efforts;
2. Determine if realistic calving can be simulated with FEA and a synthesized ram of several dimensions that is placed uniformly around the entire perimeter of an ice island ("uniform ram");
3. Determine if realistic calving can be simulated using FEA with a synthesized ram of several lengths that is placed only along the edge of the ice island that calved in the CI2D3 database ("localized ram");
4. Determine the ram dimensions (length and extent along the ice island edge) required to cause a calving event in the modelled ice islands;
5. Empirically model relationships between stress magnitude/calving events and the morphological data of the modelled ice islands.

The mechanisms by which ice islands calve are considered a significant knowledge gap, that, if filled would be highly beneficial to those in the shipping and offshore oil

industries. This knowledge can be combined into a comprehensive operational drift and deterioration forecasting model that would help predict ice island behaviour at sea.

1.2 Structure of this thesis

This thesis follows a traditional thesis format. A review of literature concerning ice island physical characteristics, drift and deterioration mechanisms, prior calving models as well as background on FEA is provided in Chapter 2. Chapter 3 describes the methods used to achieve the research objectives and Chapter 4 provides the results. Chapter 5 discusses the implications of the results, compares them to prior modelling work, and identifies the key findings of this thesis. The final chapter provides an overall conclusion and identifies further avenues for research.

2.0 Literature review

2.1 Ice island morphology

Ice islands are large, tabular icebergs with vertical sidewalls and surfaces at a constant height above sea level (Dowdeswell and Jeffries, 2017; Hattersley-Smith, 1962) (**Figures 2.1 and 2.2**). They are the largest type of iceberg defined by the Canadian Manual of Ice (Canadian Ice Service, 2005) and have a surface area of several hundred square metres to hundreds of square kilometres (Joint Technical Commission for Oceanography and Marine Meteorology, 2015). In contrast, Antarctic ice islands are referred to as "tabular icebergs" and can be several thousand square kilometres in area (Stern et al., 2017). Arctic ice islands reach thicknesses of up to 200 m but Antarctic ice islands can reach thicknesses of up to 500 m (Kristensen, 1983; Orheim, 1980). Thickness also varies according to source: ice islands from the ice shelves along the northern coast of Ellesmere Island in Nunavut are typically about 50 m thick while those from floating glacier tongues in northern Greenland may be twice that (Dowdeswell and Jeffries, 2017; Joint Technical Commission for Oceanography and Marine Meteorology, 2015). Ice islands within Arctic Canada are produced from only two areas: the ice shelves fringing northern Ellesmere Island and floating ice tongues along the northwestern coast of Greenland (Crawford et al. 2016; Jeffries 1992) (**Figure 2.3**). In the past, they have been known to drift around the Arctic for up to a decade before completely deteriorating, but today, most ice islands survive for up to only a few years (Crawford et al., 2018b; Kristensen, 1983; Van Wychen and Copland, 2017).



Figure 2.1: Photograph of an ice island ("PII-A-1-f") grounded at $67^{\circ} 21.4' \text{ N}$, $63^{\circ} 15.2' \text{ W}$, approximately 40 km to the southeast of Qikiqtarjuaq, NU. This is a fragment of the 2010 Petermann glacier calving event which measured $\sim 4 \text{ km}^2$ in September 2018 around the time of the photograph. Note the constant height above sea level and vertical sidewalls. Photograph taken by the author.

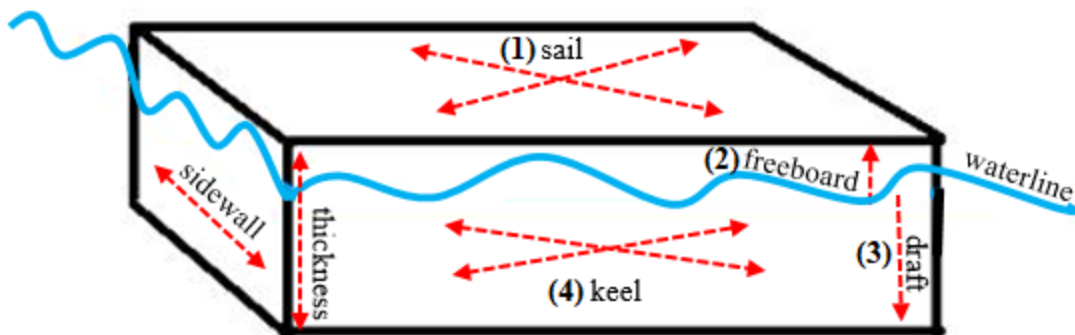


Figure 2.2: Diagram of an ice island. Its different components are indicated by red arrows and accompanying text. The sail is the mass that remains above the waterline (1); the freeboard is the height of the ice island sidewall above the waterline (2) while the draft is the vertical depth below it (3). The keel is the mass submerged below the water (4). Adapted from Crawford (2013).

Far less abundant than icebergs, ice islands were only discovered in the Arctic several decades ago. The first credible observation was made by Soviets aboard the *Krestianka* in the Chuchki Sea in 1934, and a number of additional sightings were made during reconnaissance operations in the late 1930s (Belkin and Kessel, 2017). During the Cold War, the Soviets and Americans set up semi-permanent camps on ice islands and used them as drifting research platforms (Althoff 2017; Jeffries 2002). For example, Canada installed a station on “Hobson’s Choice”, an ice island originating from the Ward Hunt Ice Shelf in 1984 (Althoff, 2017). Hobson’s Choice and other ice island research platforms helped collect decades worth of oceanographic, meteorological, geological, and biological data (Althoff, 2017).



Figure 2.3: Calving event at Petermann Glacier (Northwest Greenland) imaged on 17 August, 2010 by Landsat 7. The initial fragment (red circle) had a surface area of 270 km² immediately following calving and gave way to many additional ice islands whose lineage and drift were recorded in the CI2D3 database. The black lines over the image are due to failure of the Scan Line Corrector from the LANDSAT-7 sensor in May 2003. Image courtesy of NASA and USGS (USGS, 2010).

2.2 Ice island drift

Ellesmere ice islands (“western ice islands”) tend to drift north of the Canadian Arctic Archipelago, towards the Beaufort and Chukchi Seas, and the Arctic Ocean, while the majority of those discharged from Greenland (“eastern ice islands”) drift south along Canada’s eastern coastline through Nares Strait to Baffin Bay and the Labrador Sea (Crawford et al., 2018b).

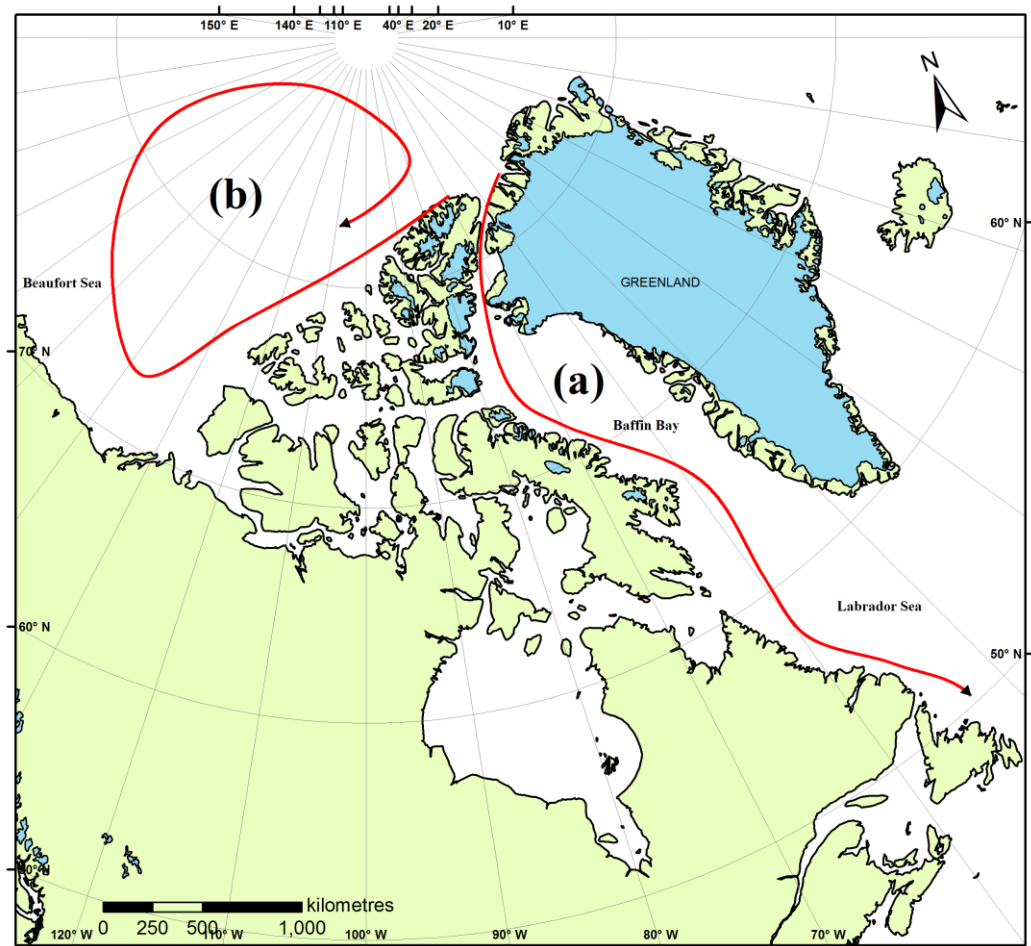


Figure 2.4: Generalized drift trajectories of eastern Canadian ice islands (a), and western Canadian ice islands (b). The blue represents glaciated regions. After Crawford, (2013) and Nacke (2016).

Greenland's Petermann and Ryder glaciers produce the majority of ice islands in eastern Canadian waters (Mueller et al., 2013). The former is particularly remarkable and has discharged massive ice islands measuring 31 km² in 2008, 270 km² in 2010, and 130 km² in 2012 (Crawford et al., 2016). Once discharged, ice islands continue to periodically calve smaller fragments (referred to as 'daughters') until they have all completely disintegrated (Crawford et al., 2018a).

Ice islands often become grounded on shoals along the continental shelf of Baffin Island and Labrador, an area sometimes referred to as "Iceberg Alley". (Bennett et al., 2013; Crawford, 2013). The shallow and uneven bathymetry along Iceberg Alley prevents many ice islands from drifting further south, and many completely disintegrate there. However, some drift further south and reach the Grand Banks region off Newfoundland.

Some shipping routes intersect ice island trajectories and ice island fragments are increasingly becoming a concern for stakeholders in the shipping and offshore oil industries (Van Wychen and Copland, 2017). Some of these potential intersections are illustrated in **Figure 2.5** for a subset of ice islands and icebergs that have been tracked via beacons and remote sensing data. Drift patterns are essential to risk assessment, but understanding of deterioration mechanisms are important to establish where and when fragments are created.

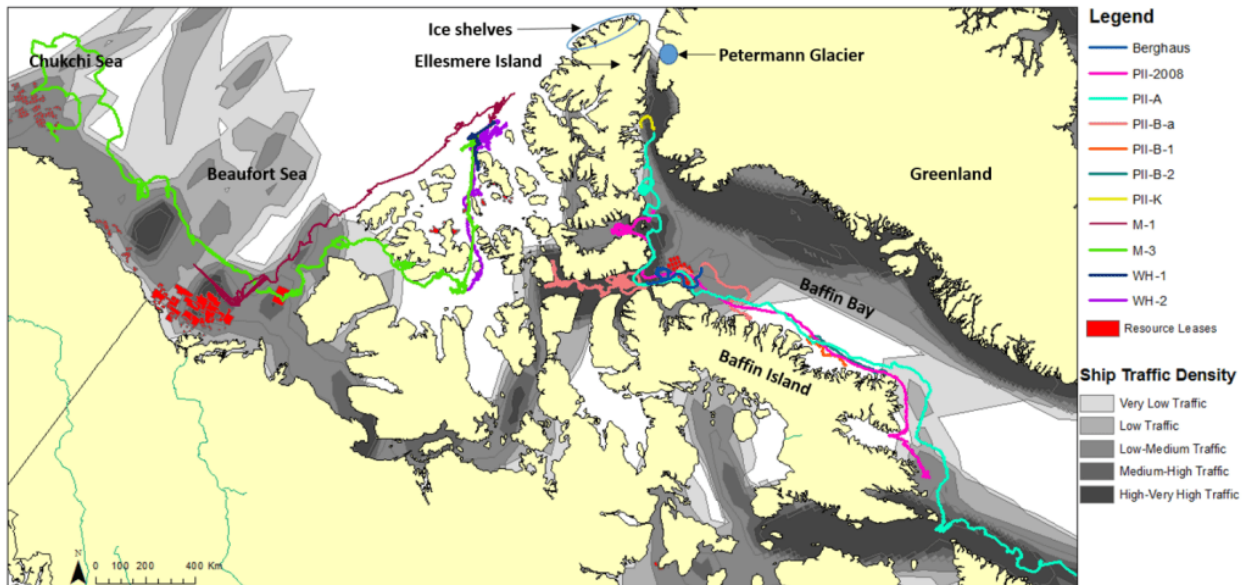


Figure 2.5: Trajectories of various ice islands and icebergs overlapping ship traffic density (greyscale legend) and oil and gas exploration leases (red). Abbreviations of parent glaciers and ice shelves are as follows: PII = Petermann (Ice Island), WH = Ward Hunt, M = Markham. Figure taken from the ArcticNet Integrated Regional Impact Studies (IRIS) report (Bell and Brown, 2018).

2.3 Ice island deterioration

Ice islands deteriorate through six main processes: 1) buoyant convection, 2) forced convection from wind and water currents, 3) wave erosion, 4) the calving of overhanging slabs, 5) surface ablation from solar radiation, and 6) large-scale fracture (or calving) events (Crawford, 2013; Savage, 2001) (**Figure 2.6**). The lattermost mechanism is often ignored due to the difficulties of modelling it (Crawford et al., 2016): many fractures are unpredictable since they propagate along internal flaws that are not detectable from remote sensing imagery. The grounding of ice islands may also lead to calving due to stresses induced from the feature it is grounded on, but these events are difficult to assess without field or bathymetry data. However, a particular type of calving mechanism

(called the “footloose” mechanism) can be predicted and is explained in subsequent sections (see **Section 2.4** and **Section 2.5**).

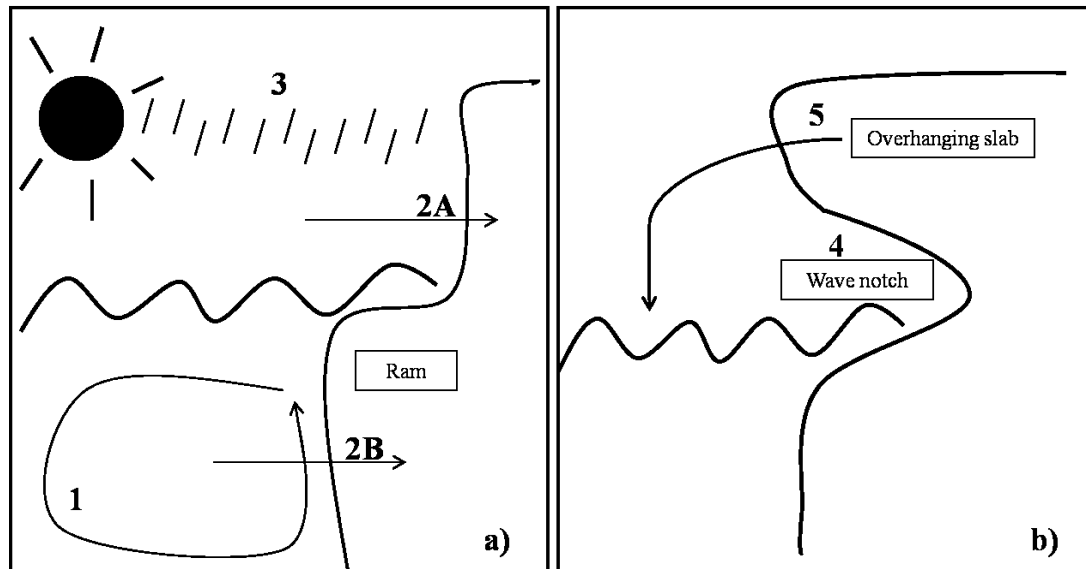


Figure 2.6: Profile view of ice island deterioration processes: 1) buoyant convection, forced convection from wind (**2A**) and currents (**2B**), melt from solar radiation (**3**), and the development of a ram (**b**) from the combined processes of wave notch formation (**4**) and the collapse of the resulting overhanging slab (**5**). Figure taken from Crawford (2013).

Most deterioration models focus on processes that cause edge-wasting events, where small fragments break off the sides of the ice island edges but do not change its shape, or the reduction of ice thickness through surface and basal ablation. Edge wasting is usually assessed from high resolution Synthetic Aperture Radar (SAR) images, which is the preferred sensor type for monitoring sea ice, glaciers and icebergs since it can image during the polar night and through cloud cover (Jawak et al., 2015; Jeffries and Sackinger, 1989). Surface area change is monitored by the digitization of ice island extents between image acquisitions (**Figure 2.7**), however, spatial resolution of the sensor can be a major limitation for monitoring these changes if they occur at the sub-resolution level (Crawford et al., 2018a). Some studies have used ice-penetrating radar

and ablation stakes to measure changes in thickness over time (Crawford, 2013; Crawford et al., 2015; Halliday et al., 2012). These observations, combined with areal extent, can be used to calculate volume loss. It is also possible to combine areal changes with satellite altimetry data (Stroeve et al., 2008; Tournadre et al., 2015) or surface/basal ablation models to infer volume change (Ballicater Consulting Ltd., 2012; Crawford et al., 2018c; Jansen et al., 2005; Kubat et al., 2007). However, most deterioration models do not account for the incidence of new independent ice fragments that are of concern to seafaring vessels (Crawford et al., 2018c, 2016; Kubat et al., 2007). These knowledge gaps should be addressed to increase the scope of deterioration modelling.

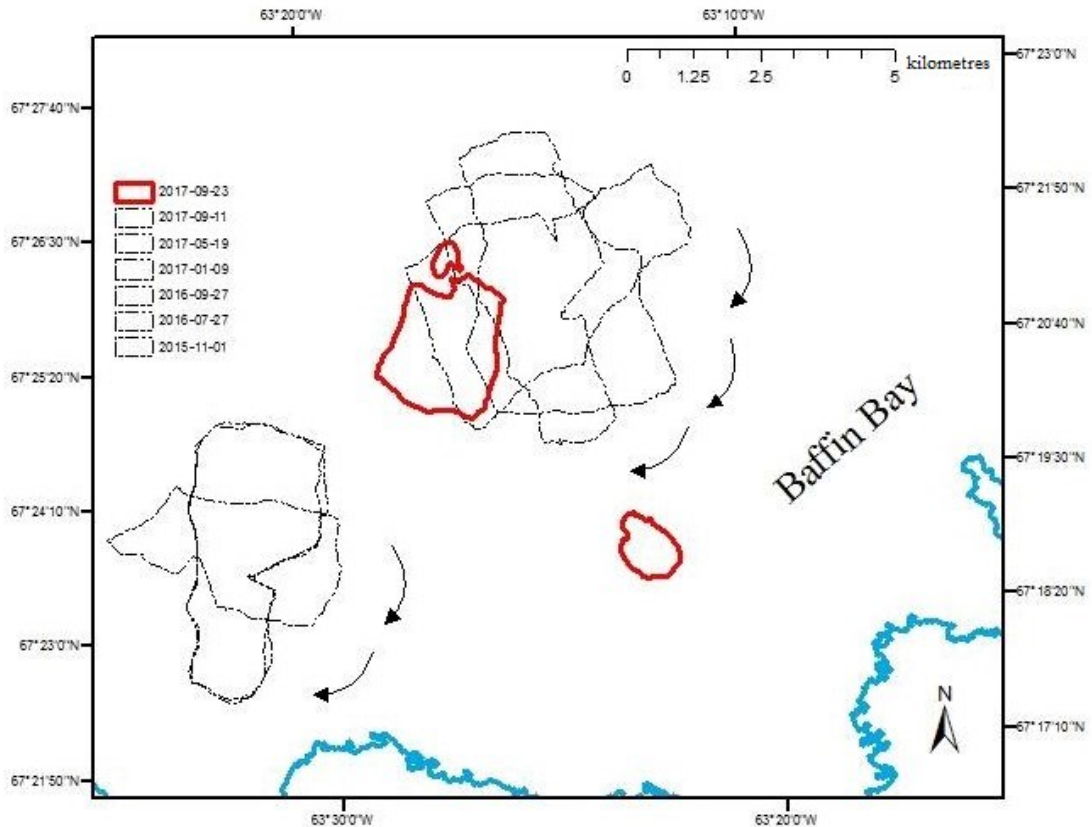


Figure 2.7: Multiple overlaid RADARSAT-2 digitizations of ice island "PII-A-1-f" between 2015-2017, showing its change in position and assumed rotation. PII-A-1-f is an ice island fragment from the 2012 Petermann Glacier calving event. The red polygon shows PII-A-1-f following its most recent calving event (Sept. 2017) and its associated daughter fragments. The arrows indicate an assumed clockwise rotation of the ice island around two grounding points. The blue lines indicate the coast of Baffin Island. All polygons were digitized from RADARSAT-2 images taken on the dates indicated in the top left of the map.

RADARSAT-2 Data and Products © Maxar Technologies Ltd. (2015-2017) – All Rights Reserved. RADARSAT is an official mark of the Canadian Space Agency

2.4 Material properties and rheology of ice islands

The deformation or failure of a material is a result of the amount of stress applied and length of time it is applied for. When relatively little stress is applied to the material, its shape may deform (called "strain"), but return to its original state when the stress is removed (elastic deformation) (Budd and Jacka, 1989; Roylance, 2001). If more stress is applied and the material strains beyond its elastic limit (yield strength), the strain becomes irreversible (plastic deformation) (Roylance, 2001). If the amount of stress the material can withstand is exceeded, the material fails, resulting in the creation of two independent fragments. The responses in strain as a function of stress are illustrated with a stress-strain curve (**Figure 2.8**).

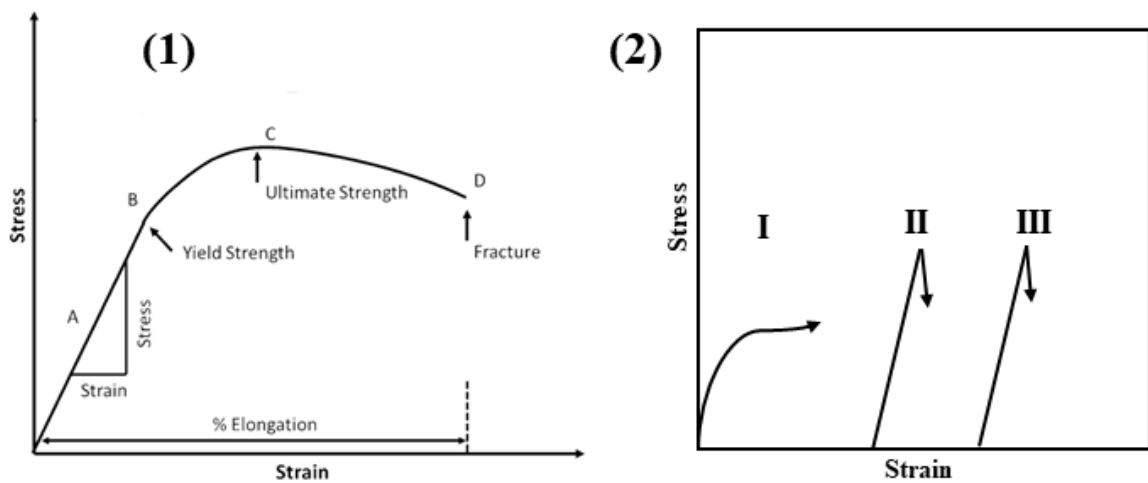


Figure 2.8: Stress and strain curves showing the different possible deformation characteristics of an unspecified material (1) and for ice under increasing rates of applied stress (2). **A** shows the elastic region, where stress and strain are proportional. The slope of this line is also the value of Young's Modulus (E). **B** is the yield strength of the material, where deformation ceases to be reversible. Beyond point **B** up to **D** is the plastic region where deformation is irreversible. **C** is the ultimate strength of the material, which indicates the maximum stress a material can withstand. **D** is the fracture point where two independent fragments of the material result (Davis, n.d.; Roylance, 2001). **I** through **III** show the behavior of ice at increasing rates of stress, indicating a plastic response when low stress is applied over prolonged time, but elastic and brittle responses applied at higher rates (2). Figure adapted from Lim and Hoag (2013) and Schulson (1999).

Ice behaves like a brittle solid, a material that reaches failure without experiencing significant elastic or plastic deformation under brief periods of high stress (Snyder et al., 2016). However, ice exhibits an elastic response when low stress is applied for short periods (Budd and Jacka, 1989). Young's Modulus (E) is the metric that describes a material's resistance to elastic deformation by the ratio of applied stress to strain:

$$E = \frac{\sigma}{\varepsilon} \quad (2.1)$$

where σ is the applied stress (Pa) and ε is the resultant strain (m m^{-1}). The higher the value, the stiffer the material. Stiffness in a material describes the load required to cause elastic deformation to occur (which should not be confused for its resistance to catastrophic material failure). For glacial ice, E ranges from values of 9.7 – 11.2 GPa at a temperature of -10°C (J. J. Petrovic, 2003; Nimmo et al., 2004). For comparison, E of a diamond is 1050 GPa or higher (Klein and Cardinale, 1993; Savvides and Bell, 1993). The elasticity and resistance to stress in a material can also be expressed with a stress-strain curve (**Figure 2.8**).

Ice also deforms plastically (referred to as 'creep') when stress is applied over prolonged periods (Glen and Perutz, 1955). Creep is observed in the advance of ice sheets and glaciers in the cryosphere, where the thicknesses of ice are so great that these features deform under their own weight and increase in extent (Duval et al., 2010). However, internal deformation of Arctic icebergs and ice islands is constrained by their limited thicknesses/weight and a lack of topographical slope to help drive this type of deformation (Nye, 1960). Thus, the effects of plastic deformation have traditionally been ignored in ice island fracture modelling (Diemand et al., 1987; Sazidy et al., 2019; Wagner et al., 2014).

The density of pure ice is 917 kg/m³ however, field measurements of glaciers and icebergs have been reported to be as low as 830 kg/m³ (Vasil'chuk, 2015) due to air and sediment impurities trapped in the ice.

When a material is stretched longitudinally, some amount of lateral contraction may occur. This change in the material's shape is described by Poisson's Ratio (ν) (**Figure 2.9**) and is calculated by:

$$\nu = \frac{-\epsilon_{lateral}}{\epsilon_{longitudinal}} \quad (2.2)$$

where $\epsilon_{lateral}$ is the lateral strain (contraction) of the material, and $\epsilon_{longitudinal}$ is the longitudinal strain (stretching) in the object. Poisson's Ratio of glacial ice is typically reported to be 0.23 to 0.45 (J. Petrovic, 2003; Voitkovskii, 1962; Gold, 1977).

The flexural strength (sometimes also called *fibre stress at rupture*) is defined as the maximum stress a material can withstand without breaking (Mandal et al., 2018) and ranges from 0.5 – 1.63 MPa in ice (Gagnon and Gammon, 1995; Wagner et al., 2014). The flexural strength of ice increases as temperature decreases. Ice is slightly more resistant to compressive forces (those that shorten a material) than tensile ones (those that elongate a material) and it is considered anisotropic, which indicates different strain rates depending on the direction of applied stress (Gagliardini, 2011). For example, the direction that stress is applied with respect to the orientation of the crystals within a fragment of ice can influence its tolerance in elastic and plastic deformation (Gagliardini, 2011).

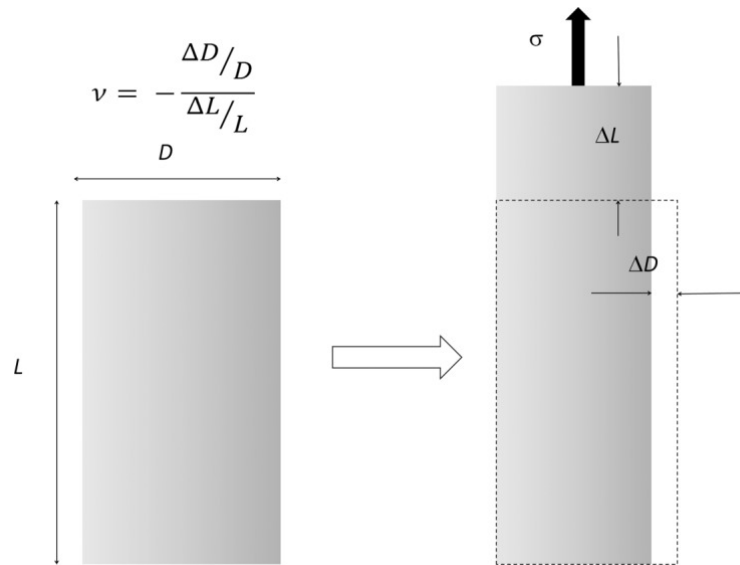


Figure 2.9: Diagram of Poisson’s Ratio of a 2-D cylinder. ΔL and ΔD indicate the negative change in its length and diameter when a tensile force is imposed on the cylinder in the longitudinal direction. ν (Poisson's Ratio) is the ratio of these changes. Figure adapted from Greaves (2013).

2.4 Buoyancy of ice islands

Archimedes Principle states that an ice island floating in seawater is in hydrostatic equilibrium because the force of gravity (F_g) pulling the ice island downwards is exactly counteracted by the buoyant forces pushing it up (F_b) (Heath, 1897). When the shape of the ice is perfectly tabular (e.g. vertical sidewalls and no ram), the hydrostatic forces acting on the bottom surface of the ice island will be equal across its surface area, minimizing the accumulation of stress. The force of gravity (F_g) is calculated by:

$$F_g = ma \tag{2.3}$$

where m is mass of the object and a is the acceleration due to gravity on Earth (9.8 m s^{-2}).

The buoyant force can be calculated from:

$$F_b = \rho_w g V_f \quad (2.4)$$

where ρ_w is the density of water and V_f is the volume of displaced fluid resulting from the submersion of the ice island. Assuming a perfectly tabular ice island shape, the buoyant force per unit area (hydrostatic pressure (P_{hs})) can also be found with the following:

$$P_{hs} = \rho_w g h_z \quad (2.5)$$

Where h_z is the height of the waterline above the draft.

The buoyancy of ice and hydrostatic pressure is thought to play an important role in ice island calving events due to the differences in the forces caused by ice rams that form below the waterline as described in the following sections.

2.5 The ‘footloose’ mechanism

Exposure of ice island sidewalls to waves leads to the formation of a notch into the ice at the waterline, which grows until the overhanging ice can no longer be supported and breaks off (Wagner et al., 2014). This creates an underwater terrace called a "ram" which increases in size as the surface of the ice island sail shrinks from the progressive edge-wasting of the notch (Wagner et al., 2014).

The development of a ram along the ice island edge results in a local hydrostatic disequilibrium as the completely submerged ram attempts to float up, causing a bending stress near the bottom edge of the ice island. If the ram is of sufficient length, extent, and thickness, localized stresses may exceed the flexural strength of the ice and result in material failure from flexure. If the resultant fracture propagates upwards to the surface of the sail, two independent ice fragments are created.

In sea ice-free water, rams can be observed by sight from ships or aircraft, and they can be measured below the ocean surface with multi-beam sonar instruments. Antarctic ice islands with rams were also detected with the Geoscience Laser Altimeter System (GLAS) which was carried by the now-defunct ICESat-1 satellite mission (Scambos et al., 2005). The increased height of the freeboard along ice island edges was thought to be a result of the upwards deflection of the ice caused by an adjoining ram.

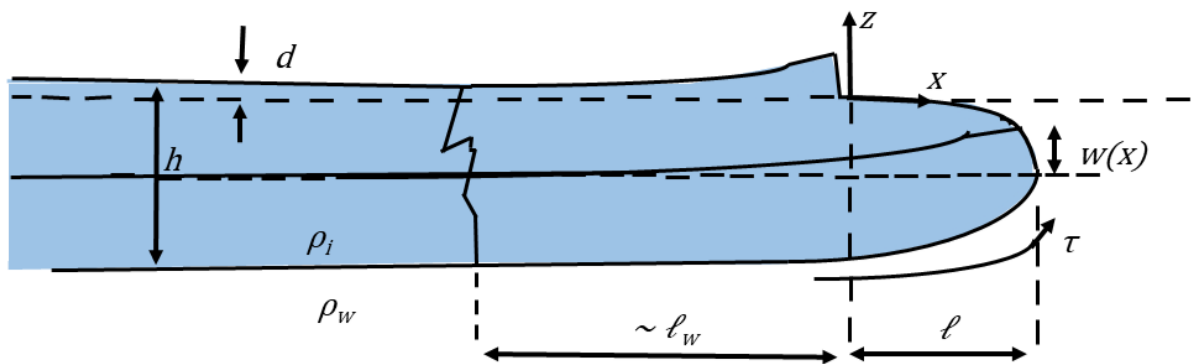


Figure 2.10: Diagram of the ‘footloose mechanism’. A ram, of length ℓ is formed as the sail (of freeboard d) is eroded over time by waves. The ram is held below its hydrostatic equilibrium by the central ice island, causing an upward bending of the ice edge. Fracture occurs where the bending stress concentrates at a distance of ℓ_w from the edge of the ice island sail. $w(x)$ indicates the upward deflection of the ice island edge that has been observed from ICESAT profiles of Antarctic ice islands (Scambos et al., 2005) P_i is the pressure of ice and P_w is the pressure of water. Figure adapted from Wagner et al. (2014).

Ice islands in warm, sea ice free water can experience ram growth $> 1 \text{ m d}^{-1}$, making ram-induced fracture a fast-developing calving mechanism (Wagner et al., 2014). It has been estimated that ice island rams in the Antarctic do not exceed lengths of 70 m, suggesting that there is a maximum ram length threshold to induce calving (Wagner et al. 2014).

Wagner et al. (2014) produced a 2-D analytical model for ice islands as an idealized elastic beam with a constant flexural strength and Young’s Modulus of 9 GPa. The model predicts the location and maximum stress along the length of the beam. The footloose

mechanism has also been extended to glacier calving front models to show they may calve icebergs when they have a submerged protrusion similar to a ram (Wagner et al., 2016). Recently, Sazidy et al. (2019) developed a 3-D version of the Wagner et al. (2014) model using an FEA approach (see **Section 2.5** and **Section 3.0**). This can be used to explore the effects of the footloose mechanism on ice island models derived from realistic shapes.

2.6 Previous calving models

In addition to Wagner et al. (2014), Sazidy et al. (2019) and Diemand et al. (1987) have described analytical methods to model the effect on stresses of these forces in 2-dimensions: one for a semi-infinite beam on elastic foundation with a localized ram, and ice islands with a perfectly symmetrical ram along opposite sides of its keel, respectively. For a semi-infinite beam on elastic foundation, the upward buoyancy load (N/m^{-1}) can be derived from (Sazidy et al., 2019):

$$P_1 = l_r h_k (\rho_w - \rho_i) g \quad (2.6)$$

Where l_r is the length of the ram, h_k is the height of keel draft, and ρ_i is the density of ice.

The maximum bending stress (σ_{max} (Pa)) can be calculated with (Sazidy et al., 2019):

$$\sigma_{max} = 0.644 \frac{E}{(1 - \nu^2)} \frac{P_1 \beta^3 h}{\rho_w g} \quad (2.7)$$

The parameter β (m^{-1}) can be estimated from the following equation (Sazidy et al., 2019):

$$\beta = \left[\frac{\rho_w g}{4} \frac{12(1 - \nu^2)}{E h^3} \right]^{\frac{1}{4}} \quad (2.8)$$

While the distance from the ice island edge where maximum bending stress (X_{max} (m)) occurs can be found from (Sazidy et al., 2019):

$$X_{max} = \frac{\pi}{4\beta} [m] \quad (2.9)$$

For a 2-D iceberg with a symmetrical ram fringing both sides, peak stresses (Pa) are likely to occur at the centre of the iceberg and can be derived by the following (Diemand et al., 1987):

$$\sigma = \frac{3l_2(l_1 + l_2)}{(h_1 + h_2)^2} h_2 g(\rho_w - \rho_i) \quad (2.10)$$

Where l_1 is the length of the sail, l_2 is the length of the ram, h_1 is the freeboard, h_2 is the draft, and ρ_i is the density of ice.

Sazidy (2019) developed two models with the FEA software package LS-DYNA to enable footloose predictions by calculating maximum principal stresses of ice islands in 3-D (described further in **Section 3.0**). Principal stress is defined as the normal stress calculated at an angle when shear stress is equal to 0 (Cuffey and Patterson, 2010). This model produced realistic results and was found to be in agreement with both of the analytical models described above (Sazidy et al., 2019). The model parameters selected and validated by Sazidy et al. (2019) are shown in **Table 2.1**.

Table 2.1: Parameter values for the ice island calving FEA developed by Sazidy et al. (2019).

Parameter	Value	Unit
Ice density (ρ_i)	900	kg/m ³
Young's Modulus (E)	9	GPa
Poisson's Ratio (ν)	0.33	unitless
Water density (ρ_w)	1024	kg/m ³

2.7 Finite Element Analysis

The Finite Element Analysis (FEA) is a numerical approach used to study the behaviour of an object subjected to forces, heat, the flow of fluid, and other physical effects (Fagan, 1992; Autodesk, 2019). In an FEA, an intricate domain is made computationally manageable by dividing it into a series of smaller, simpler shapes called *elements* in a process known as 'meshing' or 'discretization' (Nikishkov, 2004) (**Figure 2.11**). Elements are interconnected at vertices ("nodes") so that all elements that comprise the domain are topologically related (Fagan, 1992; Knowles, 1984). Governing equations are determined for solving the distribution of an unknown variable (such as stress or heat/energy flux) throughout each element (Bathe, 2014; Holland, 1974). The solved element matrices are then substituted into a global matrix, which then describes the distribution of the variable throughout the domain as a whole (Holland, 1974; O'Brien, 2010). Solutions at the element level can be determined at integration points or as an average of the nodal values. The results of the model can be visualized as an animation and a colour scale is typically used to view the distribution of the variable of interest throughout the mesh over time.

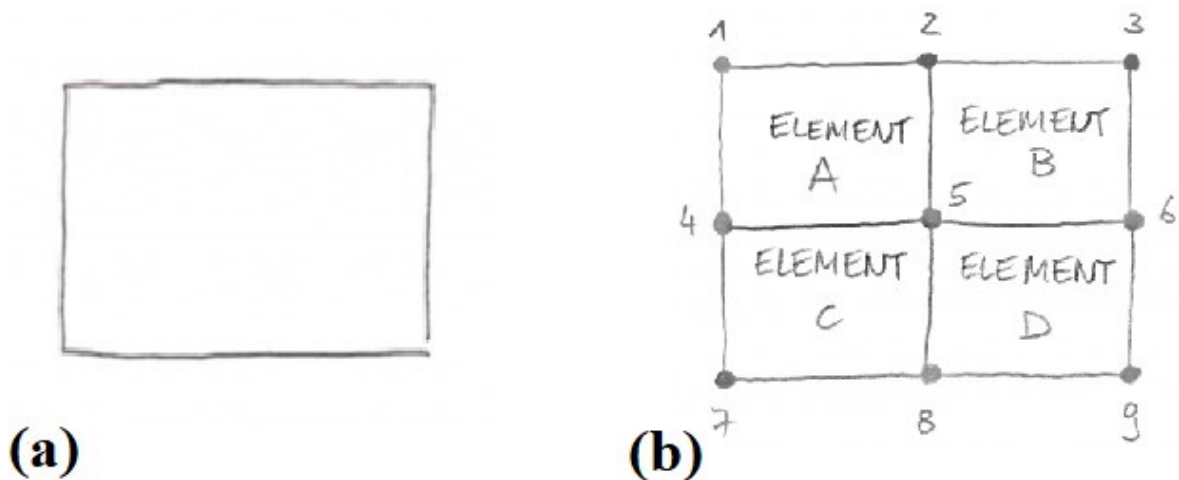


Figure 2.11: A simple 2-D rectangular domain (a) and its mesh divided into 4 elements whose extents are delineated by 4 nodes each (b). The interpolation function for these elements is linear since there are only two nodes between opposite ends of each element (corresponding to two terms). Elements are indicated by letters A-D and nodes are numbered 1-9. Figure adapted from (Skotny, 2019).

The FEA process requires a geometric solid (or body) model of the domain to be studied (Burkardt, 2011). These are created with FEA meshing software packages interactively or in third-party computer-assisted design (CAD) software that exports models file formats recognized by major FEA software packages (Geuzaine and Remacle, 2019). The model is then meshed to a desired element shape and resolution within an FEA software package.

Elements can comprise any shape delineated by a series of nodes. They may be a simple line (1D), square/rectangular, or triangular (2-D) or tetrahedral or hexahedral shapes (3-D) (Abaqus, 2017) (**Figure 2.12**). Triangular or tetrahedral elements are more efficient for meshing intricate shapes but are generally less accurate for deriving solutions than rectangular or hexahedral elements (Wang et al., 2004). A balance between mesh computation time and solution accuracy must be struck.

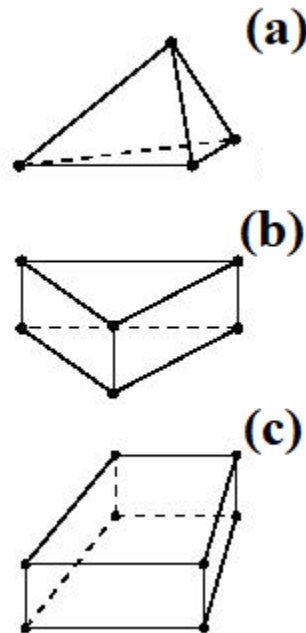


Figure 2.12: Types of 3-D elements; 3-D tetrahedron (a & b) and hexahedron (c) elements are each shown with linear shape functions. Figure adapted from Abaqus (2017).

Higher element and nodal resolutions also increase solution computation time because the number of nodes between element faces is equal to the number terms present in the element interpolation function (Nikishkov, 2004). Similarly, the time step (frequency) for which solutions are calculated also dictates the duration of processing, with finer time steps taking longer. If the time step value is too coarse, important results (such as a maximum stress or temperature) may be aliased entirely between calculations. The time step can also be automatically optimized according to element mass in a process known as “mass scaling” (LS-DYNA, n.d.). Users strike a balance between element size, node quantity, and the solution time step so that a reasonably accurate result can be achieved in a minimal timeframe.

To produce FEA model results, meshes are assigned material properties, boundary conditions, forces, and the calculation time step as parameters before the model file is ingested into a solution program. The results of the FEA model are output as a series of new files which can be visualized in the program's graphical user interface as a 3-D animation. Output tables may also be generated. One of the major advantages of FEA is the ability to complement quantitative results with visualizations.

FEA is popular in studies of ice front calving in glaciers and ice shelves (Fastook and Schmidt, 1982; Iken, 1977; Mobasher et al., 2016; Trevers et al., 2019) but there have been limited studies where the technique has been applied to ice island or iceberg calving events. Since large-scale ice island calving events share many of the same mechanisms and parameterizations as FEA glacier calving models (Fastook and Schmidt, 1982; Trevers et al., 2019; Hanson and Hooke, 2000), using it as an approach to model these features is a reasonable next step. FEA is ideally suited to deal with the irregular shapes of ice islands that are caused by the constant erosion of the sidewall and episodic calving events, which cannot be accurately represented in idealized 2-D analytical models.

3.0 Methods

Objective 1 of this thesis was met by collecting *in situ* thickness measurements of an ice island fragment of the 2012 Petermann Glacier calving event that was grounded near Qikiqtarjuaq, NU during the 2018 annual Amundsen Science cruise (**Section 3.1**). The remaining objectives were met by selecting 2-D outlines of ice island polygons from the CI2D3 database that fractured in a manner similar to the footloose mechanism (**Section 3.2**) and converting them to a 3-D shape (**Section 3.3**). Stresses associated with buoyancy forces were predicted using FEA. A ram of a given length was created uniformly around the ice island model using a custom script (**Objective 2**). Another version of the ice island was created with a ram localized to the edge that broke off from the mother ice island (**Objective 3**). The propagation of a crack was simulated using an element erosion method with a flexural strength threshold (Sazidy et al., 2019). Results were analyzed by visualizing the simulated stress over time in the LS-PrePost graphical user interface. Later, the flexural strength threshold was removed and the maximum of maximum principal stresses (MPS) of each ice island were simulated (**Objective 4**). These data were then used to produce empirical models that predict stress magnitude as a function of ram and ice island morphology (**Objective 5**).

3.1 Ice island nominal thickness estimation

To estimate a mean nominal thickness parameter for **Objective 1**, *in situ* thickness measurements of an ice island fragment from the 2012 Petermann Glacier calving event ("PII-A-1-f") were collected with a 25 MHz mobile Ice-Penetrating Radar (mIPR) (Blue System Integration Ltd.). PII-A-1-f, then located at approximately 67° 21.4' N, 63° 15.2'W (**Figure 2.1**) was accessed by helicopter from the *CCGS Amundsen* on the

morning of September 1st, 2018. A ~ 4.5 km survey transect was completed with the mIPR, which calculates the two-way travel time of radio waves travelling from the transmitter to the ice-water interface (and back to the receiver), and converts the recorded distance to metres. A mobile GPS unit (TopCon Hiper V, Topcon Corp., Tokyo, Japan) was attached to the mIPR system and recorded the positions of each thickness measurement (see Crawford et al., 2019 for further details on mIPR methods and a description of PII-A-1-f). The thickness data was plotted on a RADARSAT-2 image of PII-A-1-f taken on the same day as the survey in order to produce a spatially-referenced thickness profile of the ice island. The mean thickness of the entire transect was also calculated.

3.2 Ice island selection

The CI2D3 database (V1; https://www.polardata.ca/pdcsearch/PDCSearch.jsp?doi_id=12678) catalogued the drift and deterioration of ice islands from three major calving events from Petermann Glacier and other floating ice tongues of northwestern Greenland (Ryder, Steensby, and CH Ostenfield glaciers) (Crawford et al., 2018a). The database contains over 25,000 ice island polygons traced from RADARSAT-1, -2 and ENVISAT satellite images as they drifted from Nares Strait to as far as Newfoundland (Crawford et al., 2018c). Each observation has a unique ID field (“inst”) and is related to its parent ice island (a concept referred to as “lineage”). When an ice island calves, both fragments are considered to be ice islands with unique names, a convention that is used throughout this thesis. Other attribute fields are included in CI2D3, such as surface area, length, source ice tongue, and whether the ice island was grounded, trapped in sea ice, or free-floating.

The CI2D3 database was queried for all ice island observations that underwent calving in their subsequent database entry, according to the lineage relationship ($n = 336$). The 2-D polygon of each ‘mother’ ice island was plotted along with the two or more ‘daughter’ fragments that were subsequently produced to visualize the results of each fracture event in a “calving plot” (e.g., **Figure 3.1**). These were analyzed qualitatively to eliminate all fracture events that were not relevant to this study. For example, ice islands that fractured near the centre were discarded since this mode of calving is thought to result from large internal flaws unrelated to the footloose mechanism (Diemand et al., 1987). Only mothers that calved near their edges and produced a daughter fragment that was approximately 20% or less of the surface area of the mother were retained (**Figure 3.1**). Ice islands trapped in sea ice or grounded ($n = 11$) were discarded, since calving may have been influenced by substantial non-hydrostatic loads which fall outside the scope of this study.

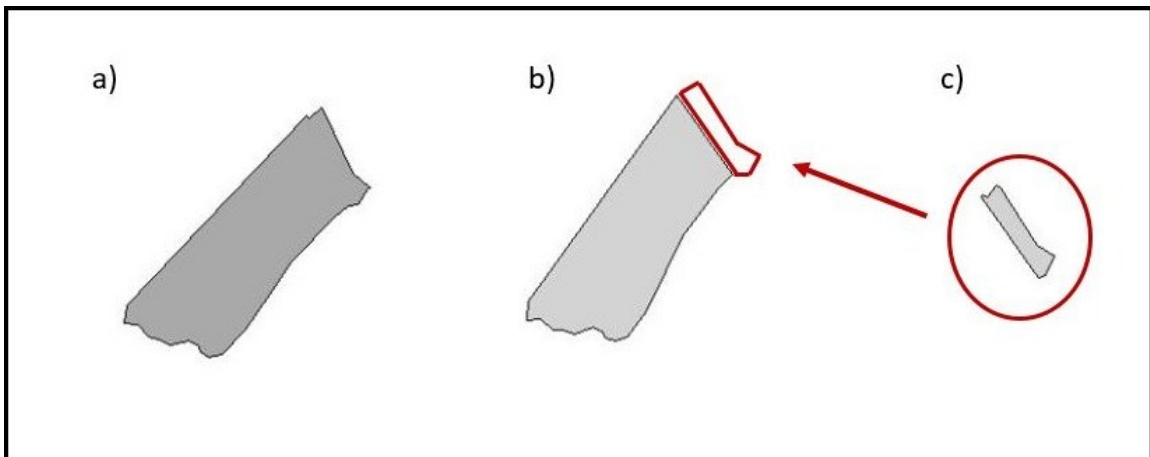


Figure 3.1: Sample ‘calving plot’ of instance “20101106_113811_r2_12_LWI” (a). A fracture near its northeastern edge resulted in daughter instances (b) and (c). The mother polygon is represented in dark grey on the far left of the plot with the daughters shaded in light grey to the right.

To reduce mesh processing to a reasonable computational time, the ice island subset was further reduced to ice islands with a length of ≤ 7.5 km ($n = 23$).

3.3 Meshing and ram creation

A custom workflow in R (Version 3.3.2), a programming language for statistical computing and graphics generation (R-Project, 2019) was used in conjunction with LS-DYNA PrePost (a software program that creates meshes and visualizes FEA model results from LS-DYNA Solver) to pre-process the polygons of ice island extents into 3-D meshes. The scripts used in this thesis project to process and solve ice island meshes may be accessed from <https://github.com/jsmith2-wirl/icemesher>.

The 23 selected ice island 2-D polygons were extracted from the CI2D3 database using R, buffered by a prescribed ram length (m) and converted to a “K” file (*.k), a text-based format that LS-DYNA can ingest. Three ram lengths were prescribed for each experiment: 20, 40, and 60 m. The 2-D shape was meshed at a 20 x 20 m resolution in LS-DYNA (*meshsize (m)*) and extruded to a nominal thickness of 80 m (*zlength (m)*) at a *meshsize* of 10 m by running PrePost non-interactively via the R script (**Figure 3.2**). The 80 m thickness parameter was utilized based on averages cited in the literature (**Section 2.3**) and the survey of PII-A-1-f completed in September 2018.

The resulting mesh K file was opened and a concave hull function (from the R package *concaveman* V1.0; using the default concavity setting) was used to identify vertices along the perimeter of the uppermost surface of the mesh. Mesh elements in the top layer were deleted along the periphery of the ice island inward to correspond with the ram length (equivalent to the polygon buffer distance) (**Figure 3.3**). All nodes that were not referenced by the remaining elements were deleted from the mesh to guarantee a stable solution (LS DYNA, 20117). This resulted in an ice island mesh with the top of the synthesized ram occurring at its natural waterline (**Figure 3.2**).

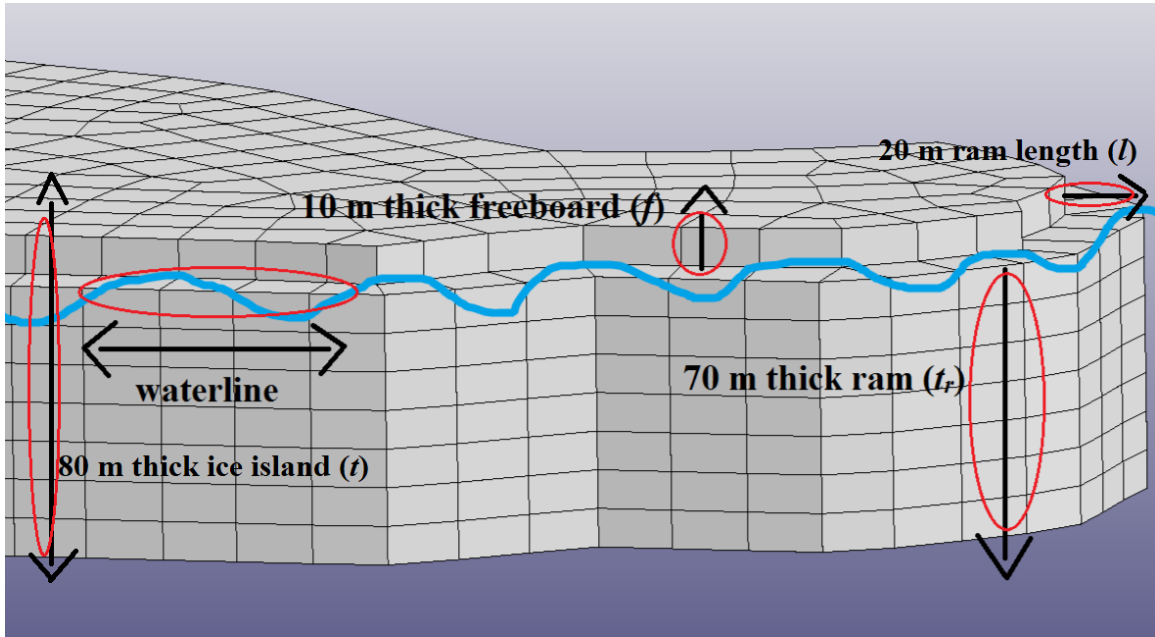


Figure 3.2: Profile view of a sample ice island mesh. The freeboard is 10 m (f) and the submerged sidewall/ram measures 70 m thick (t_r). For an ice island of 80 m thickness, the top of the ram floats at approximately the waterline (indicated by the blue line) given a water density of $\rho_w = 1024 \text{ kg/m}^3$ and an ice density of $\rho_i = 900 \text{ kg/m}^3$.

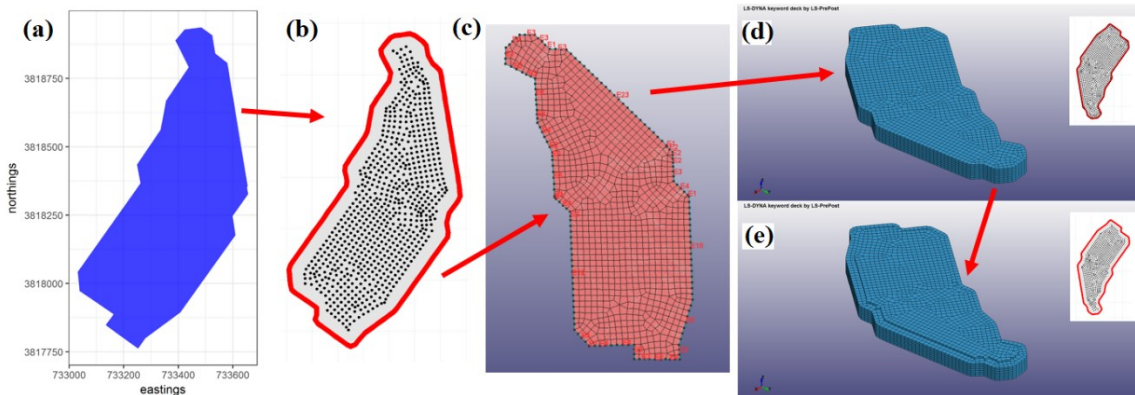


Figure 3.3: The polygon to 3-D ice island mesh process. (a) shows the CI2D3 polygon plotted on to a Cartesian grid and (b) shows the same polygon as a series of nodes with a 40 m buffer drawn around it. (c) shows the resultant 20 x 20 m mesh. The mesh is extruded into 3-D ($t=80 \text{ m}$) (d) and nodes within the 20, 40, or 60 m buffer are removed to create a symmetrical ram surrounding the ice island (e).

3.4 Material properties, forces, and simulation settings

Several required FEA parameters were defined and organized within K files as ‘cards’ (model parameter sections within K files) so they could be interpreted by the FEA software (LS-DYNA, 2007). A simple text file containing all of the model parameter cards was pasted into each K file (**Table 3.1**). The segment set (the plane at the bottom surface), height of the ice island waterline, and damping coefficient are variables unique to each mesh and were derived independently for each ice island (see section **3.4.1** and **3.4.2**). In addition to the dimensional parameters mentioned above, parameters describing the material properties of ice (ρ_i , ρ_w , E , ν , σ) and the simulation (termination time, timestep, tssfac) were pasted into these cards either as constants or with functions written in R that determined their values. Termination time (s) is the total length of the simulation run, timestep is the interval at which the calculations are made, and tssfac is a timestep scaling factor that further adjusts the time step according to the element mass.

Table 3.1: Parameters for the FEA ice island model

Parameter name	Value	Units	Notes	Source
thickness (t)	80	m		
ram thickness (t_r)	70	m		
meshsize	20	m ²	size of mesh in horizontal	
zlength	80	m	thickness	
zelem	8	unitless	no. of elements in vertical	
density of water (ρ_w)	1024	kg/m ³		
density of ice (ρ_i)	900	kg/m ³		
Young's Modulus (E)	9×10^9	Pa	elasticity of a material	Vaughan, 1995.
Poisson ratio (ν)	0.33	unitless	ratio of longitudinal strain to lateral strain	Voitkovskii, 1960.
flexural strength of ice (σ)	500	kPa	stress threshold for material failure	Vaughan, 1995.
termination time	125	s	length of simulation run	
timestep	0.1	s	solution timestep	
timestep scaling factor (tssfac)	0.6	unitless	mass scaling factor for solution calculations	

3.4.1 Segment set and height of the waterline

Gravity and hydrostatic pressure are predicted by the FEA model. The hydrostatic pressure equation requires specification of a segment set (basal plane) to indicate the surface of loading and the position of the waterline above the segment set (Sazidy et al., 2019). Hydrostatic pressure (P_w) was calculated from equation 2.5.

Where g is the acceleration of gravity, and h_z is the average height of the ice island above the waterline. The segment set was assigned to each mesh using a custom function in R that returned the coordinates of nodes at the lowest mesh elevation. The position of the waterline above the bottom surface of the ice island was calculated based on ice volume, converted to mass (weight) based on the respective densities in **Table 3.1**, and was listed in the reference plane field (*ref-z*) of the hydrostatic curve card.

3.4.2 Damping coefficients

In oscillating physical systems, energy from resistive or frictional forces needs to be removed for the model to achieve realistic, smoothed results (LS-DYNA, 2017). This is referred to as "damping" (**Figure 3.4**) and is accomplished with a coefficient term (D_s ; unitless) whose value is related to the mass or volume of the object. D_s can be found by taking the time of two successive stress peaks in a plot of element MPS (LS-DYNA, 2017):

$$D_s = \frac{4\pi}{T} \quad (3.2)$$

where T is the difference in time between successive oscillation peaks of first principal stress in an un-damped solution.

An empirical model was derived to predict damping coefficients of the meshes to avoid fitting this coefficient to all model permutations in this study ($n = 153$) by hand (M. Sazidy, personal communication, April 22, 2019). Eight simplified rectangular meshes with volume ranges corresponding to those from the CI2D3 database subset were created and solved. Damping coefficients were plotted as a function of mesh volume, and a logarithmic-linear model was fit to these points ($R^2 = 0.96$, RMSE = 6.36) (**Figure 3.5**). The model was used to predict the correct damping coefficient and an R script pasted this value into the appropriate field of the damping card in the mesh K file.

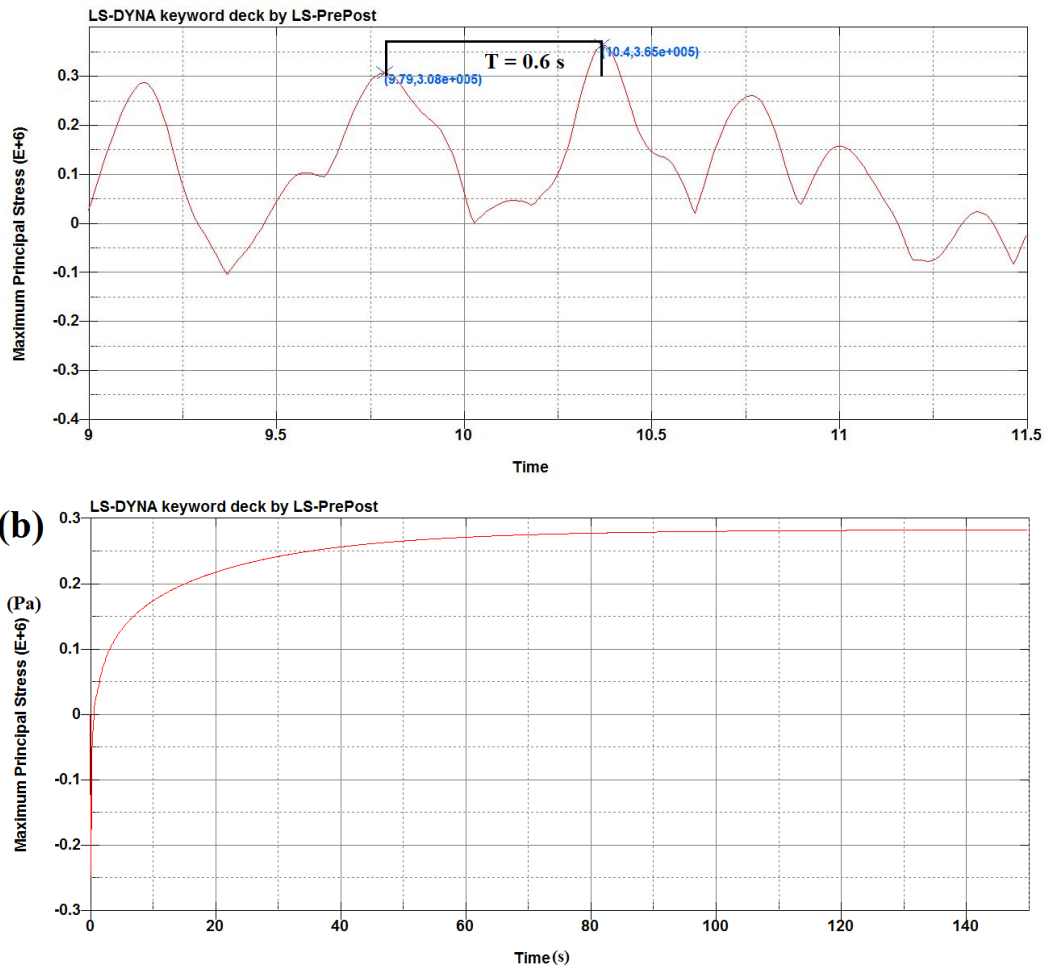


Figure 3.4: Manual determination of damping coefficients. Damping coefficients can be found by selecting two successive peaks from the sinusoidal plot of un-damped MPS history in LS PrePost (a) in order to provide a more realistic stress history (b). The time on the X-axis of two successive peaks are recorded for use in the damping formula (Equation 3.2).

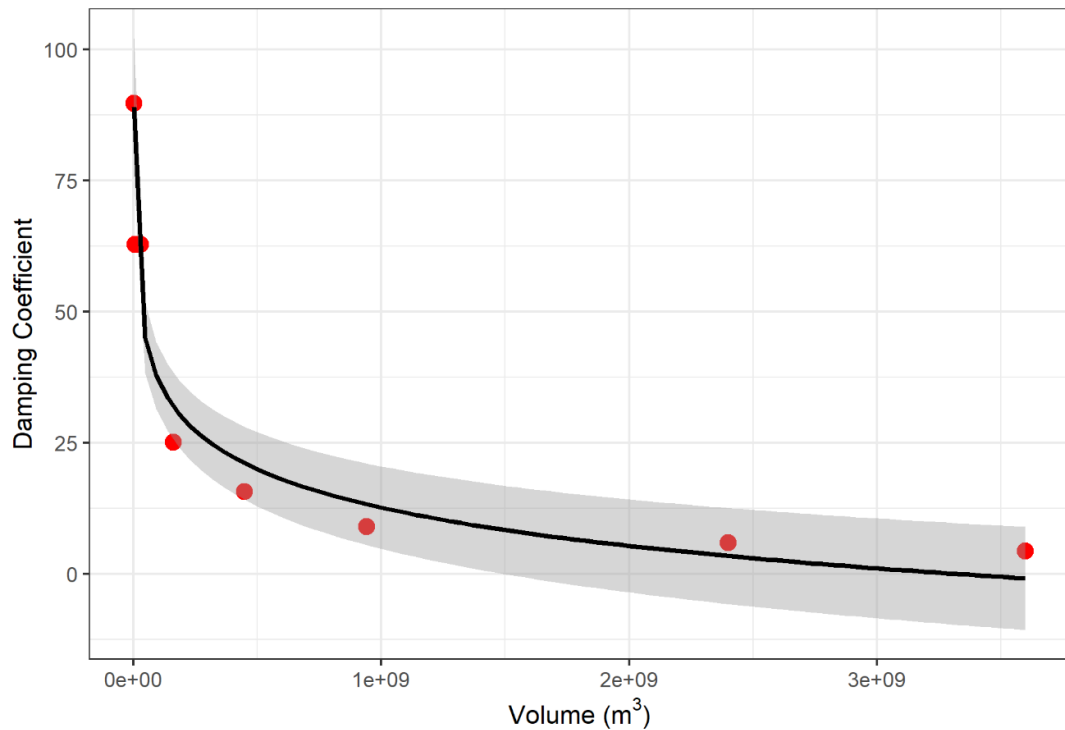


Figure 3.5: Equation to automatically determine damping coefficients ($\hat{y} = 231 - 10.5x$; $R^2 = 0.96$). A log-linear model was fit to the observation points and used to predict damping coefficients in the CI2D3 model subset. The grey area indicates the 95% confidence interval of the model.

3.5 Compiling solutions

The K files were run through LS-Solver. Solution output files (*.d3plot) were stored in sub-directories sharing the name of the modelled ice island (instance) for analysis. Each of these outputs were examined in the LS PrePost GUI later. Results from each model run were reviewed in LS-DYNA PrePost. Animations of the MPS for each mesh were viewed from different angles to observe patterns in stress distributions over time. The location and magnitude of the peak stresses, and whether the stress failure threshold was reached or not, were recorded in a spreadsheet along with general notes about the simulation results.

3.6 Sensitivity analysis

Resolution is typically optimized by selecting the coarsest resolution with minimal loss of precision (called "convergence") (Patil and Jeyakarthikeyan, 2018; Reddy, 2006). Since element resolution and aspect ratio are known to influence the accuracy of FEA results (Patil and Jeyakarthikeyan, 2018) a sensitivity analysis was conducted to evaluate if the model was robust to a variety of horizontal and vertical mesh element sizes.

A simple rectangular ice island (1040 x 480 x 80 m) with no ram was meshed at four different resolutions and each was run through the FEA model. A custom function identified the element which reached the maximum of MPS in each solution and calculated the mean MPS for all elements located within a 60 m radius of that location. The element stress histories of each of these 'peak stress zones' were aggregated into a single table and summary statistics were recorded to determine the influence of mesh size on modelled stress (**Section 4.1**).

3.7 Ram orientation analysis

CI2D3 was developed using satellite remote sensing imagery and the actual size and shape of the ice island rams remain unknown (Crawford et al., 2018a). Given that there is no available information on the ram size/shape, the ice island meshes described above were developed based on the assumption that a ram of a consistent length circled the entire perimeter of each ice island. This "uniform" ram was modelled in the first experiment to assess the hypothesis that uniform, symmetrical rams could cause a calving event that matched those inferred from the corresponding remote sensing imagery.

The hypothesis that a ram restricted to only one side of the ice island ("localized rams") is responsible for footloose mechanism type calving was addressed by synthesizing a ram along the "calving edge" of each ice island. The calving edge is defined as the edge of the ice island that is lost to the smaller daughter fragment following the calving event. The calving edges of each ice island were identified by examining the calving plots of the mother ice island and associated daughter fragment(s). The coordinates at opposite ends of the calving edges were passed to a custom function that computed a line between ends, and then deleted all elements associated with the ram (as described in **Section 3.3**) along the perimeter not belonging to the calving edge (**Figure 3.6**). This resulted in a localized ram adjoining only the calving edge (**Figure 3.7**). The distance that the ice island ram measures along the ice island edge is referred to as the ram extent.

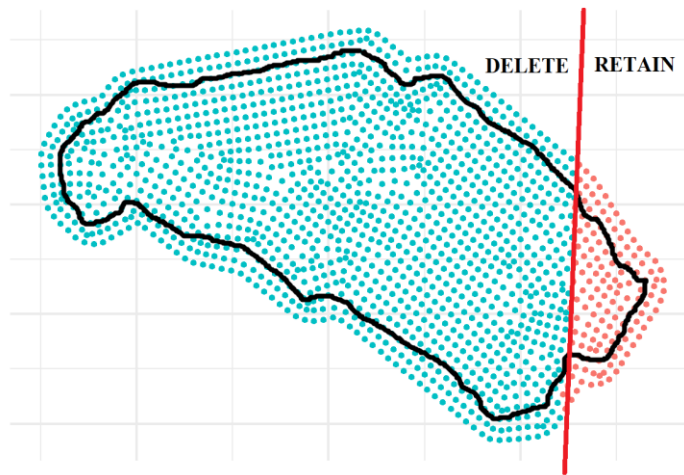


Figure 3.6: Creation of a localized ram on ice island “20120911_115220_r2_1_IKY”. The surface extent of the ice island instance is delineated with a black outline. The original 40 m long uniform ram is represented by the points laying outside of the border. The calving edge was isolated by computing a line (red line) between each extent of the calving edge. Then, the elements outside the surface extent of the ice island were deleted, leaving a localized ram along only the calving edge.

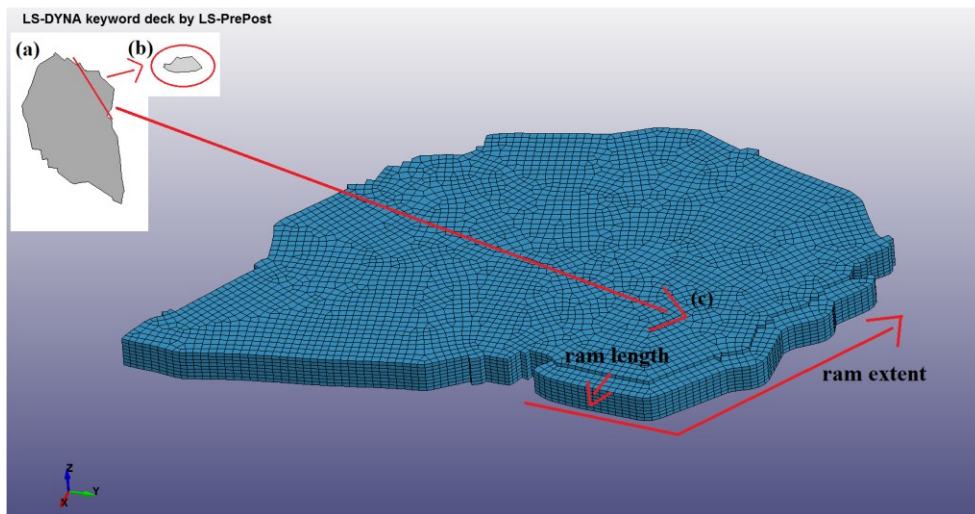


Figure 3.7: Example of an ice island mesh (“20110705_214859_r1_0_BSS_20”) with a ram length of 60 m localized to the calving edge (c). The inset at the top left shows the CI2D3 mother polygon with a red line indicating the assumed calving edge (a) and the daughter fragment that resulted from calving (b). Ram length and ram extent are indicated with arrows.

Each mesh was passed through LS-Solver and the simulation results were recorded in a spreadsheet in the same manner described in **Section 3.5**. Total ice volume and the extent of the ice island rams along with the percentage of total ice volume contained within the ram were also recorded. These were calculated based on modelling parameter assumptions, where $t = 80$ m, $t_r = 70$ m, and rams of lengths 20, 40, and 60 m. The length of the extents of the rams were estimated with the length and ram volume parameters.

3.8 Reduced localized ram extent analysis

To explore the potential role of ram extent in calving events, a subset of $n = 5$ random ice islands were selected from the initial ice island modelling sample and given a ram of half the extent of the original localized ram. This was accomplished by deleting half of the elements associated with the ram with half of these deletions occurring on each end of the localized ram, respectively. Only five ice islands were selected due to the laborious nature of manually deleting elements. These models were solved and results were recorded into a spreadsheet in the same manner described in **Section 3.5** and **Section 3.7**.

3.9 Limitless flexural strength analysis

All ice island meshes with localized rams (including those with a shortened ram extent) were modelled in LS-Solver with a limitless flexural strength by disabling the element erosion method (Sazidy et al., 2019). A custom function was written in R to write the maximum of MPS to a table along with the name, total ice volume, ram length, ram volume, ram extent, and the percentage of total ice volume contained within the ram of each ice island permutation.

3.10 Empirical modelling

The data derived from the limitless flexural strength analysis (**Section 3.9**) were used to statistically model relationships between ice island morphological traits and the MPS magnitude. MPS, ice island volume, volume of the ram, ram extent, and the percentage of total ice volume contained in the ram were examined for normality using histograms, QQ-plots, symmetry (skewness) and the Shapiro-Wilk test. Variables that were not normally distributed were transformed and then re-examined as above.

The relationship between MPS and each of the variables was assessed with a series of plots, linear models, and correlation matrices. Five FEA model results were removed from the dataset since they had $MPS > 1.67$ MPa, which is the upper limit for ice flexural strength identified in the literature (Gagnon and Gammon, 1995).

To maximize the skill of the model, a Variance Inflation Factor (VIF) test was run on a maximal multiple regression model (one that included all possible model variables except third-order or higher level interaction terms). The VIF indicates the amount of collinearity among the independent variables (Long et al., 2018). A VIF value = 1 indicates no collinearity and higher values indicate the proportion of variance caused by collinearity. For example, a VIF = 1.9 indicates the variable has 90% more variance than if it were not collinear with other independent variables. Variables with VIF values above a robust threshold (VIF of 2) were removed from the model (Zuur et al., 2010).

A backwards stepwise Multiple Linear Regression (MLR) was performed from the maximal model to assess variable significance with respect to MPS. Backwards stepwise regression is used to produce a model that maximizes explanatory power while retaining

the fewest possible parameters (most parsimonious) by removing variables that are not statistically significant or cause an increase in the Akaike Information Criteria (AIC) of the model (Crawley, 2007). AIC penalizes superfluous parameters, and superior models have a lower AIC score than inferior iterations (Crawley, 2007).

To estimate prediction ability, bootstrapping ($B = 10$ sub samples) was used to calculate the Root Mean Square Error (RMSE), Mean Absolute Error (MAE), and the coefficient of determination (R^2) for each of the models in this study.

An Analysis of Covariance (ANCOVA) was used to compare the variables used in the MLR, with the ram length and total ice island variables converted to nominal data types.

An alternative ice island volume variable was created by grouping ice island surface areas into a binomial nominal variable: low ($< 4.5 \text{ km}^2$) and high ($> 4.5 \text{ km}^2$). Ram length was treated as a nominal variable with three levels (20, 40 and 60 m). All other variables were left to as continuous covariates. The model was constructed and pruned in the same manner as the MLR.

To closer examine the relationship between stress and each of the volume categories, a bivariate linear regression was performed to predict stress as a function of volume in each of the size categories (“low” and “high”).

4.0 Results

4.1 Ice island nominal thickness estimation results

Mean thickness of the ice island transect survey conducted on PII-A-1-f on September 1, 2018 was 79 m. **Figure 4.1** shows the transect route and a thickness cross-section of Line 5.

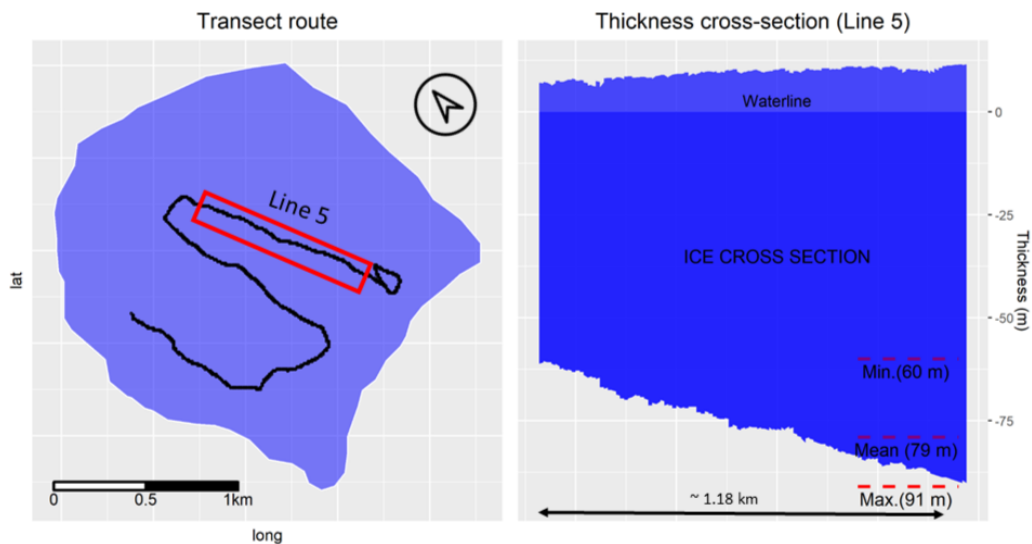


Figure 4.1: Transect results of ice island "PII-A-1-f". (a) shows the ~4.5 km long transect route from an aerial perspective with Line 5 enclosed in the red box. (b) shows the thickness profile of Line 5, with the mean, minimum, and maximum estimated thickness values indicated by the dotted red lines.

The 23 ice islands selected for this study had a waterline length of 1.2 to 6 km and were between 0.4 and 19.6 km² in surface area (**Table 4.1**). **Figure 4.2** shows a map of their distribution throughout the eastern Canadian Arctic and North Atlantic regions.

Following the typical eastern Canadian ice island drift trajectory, most ice islands were located along the eastern Canadian coastline between Nares Strait (80° 53'N) and Newfoundland (49°45'N) at the time of imaging. Seven ice islands (30%) were located in Lancaster Sound to the east of Prince Regent Inlet. These were among the largest ice islands in this study, with surface areas ranging from 9.9 km² to 14.74 km². All modelled

ice islands calved from Petermann Glacier (Northwest Greenland) except for instances "20121203_113042_r2_4_FRJ" and "20130907_112415_r2_7_CHG" which calved from Ryder Glacier in Northwest Greenland. **Figure 4.3** shows the selected ice island's ("mothers"), subsequent calved fragments ("daughters") and depicts their relative surface area in a network graph. The mean number of calved fragments produced from this subset was 2.4 with a maximum of 5 and a minimum of 2 fragments per mother. The mean surface area of calved fragments (discounting the larger fragment) was 0.23 km² with a minimum of 0.02 km² and a maximum of 0.68 km². These extents represent 1 to 9% (mean ~3.7%; **Table 4.1**) percent of the mother's original surface area.

Table 4.1: Ice islands used for fracture modelling with their pre-fracture surface area, perimeter, length, and the percentage of mother ice island surface area occupied by the daughters.

Ice island	Area (km ²)	Perimeter (km)	Length (km)	Daughter (%)	Region
20100805_160926_es_2_PYO	2.6	8.3	2.6	2.3	Nares Strait
20101106_113811_r2_12_LWI	1.8	6.6	2.4	2.2	Baffin Bay
20101107_224624_r2_5_WCZ	10.4	16.7	6.1	2.7; 1.6	Baffin Bay
20101114_224224_r2_29_ZVB	9.9	15.8	6.1	1.1	Lancaster Sound
20101203_115225_r2_4_PJJ	1.2	4.9	1.8	2.8; 2.1	Baffin Bay
20110315_211643_r1_0_QWZ	2.3	7.0	3.0	8.6; 5.9	Davis Strait
20110608_213440_r1_1_HFL	3.9	12.6	3.8	6.3	Labrador Sea
20110705_214859_r1_0_BSS	1.4	5.1	2.0	9.2	Labrador Sea
20110720_103342_r2_3_BCS	1.8	6.2	2.2	1.8	Baffin Bay
20110830_094940_r1_0_RGN	12.9	17.0	4.6	3.3; 5.3	Labrador Sea
20110910_124334_r1_0_FPS	14.7	19.6	7.0	4	Lancaster Sound
20110912_123748_r2_0_WXE	13.6	19.0	7.0	1.9	Lancaster Sound
20110923_121654_r2_0_IWV	12.6	17.6	6.6	3.2	Lancaster Sound
20110928_211932_r2_1_RFC	2	6.2	2.1	9	Labrador Sea
20111103_130828_r1_0_MUX	11.8	16.6	6.3	2.1	Lancaster Sound
20120826_125835_r2_0_XLL	11.5	14.9	5.7	3.4	Lancaster Sound
20120826_225427_r2_0_RPD	11	15.2	5.7	1.1	Lancaster Sound
20120906_123742_r2_0_VVV	10.8	14.8	5.7	1.6	Baffin Bay
20120911_115220_r2_1_IKY	0.4	2.9	1.2	5	Baffin Bay
20120930_123720_r2_0_IFE	13.2	15.4	5.7	2.2; 4.2	Baffin Bay
20121126_113605_r2_1_LJK	9.5	13.8	5.2	5	Baffin Bay
20121203_113042_r2_4_FRJ	4.9	9.8	3.8	2.8	Baffin Bay
20130907_112415_r2_7_CHG	4.7	9.4	3.1	4.4	Baffin Bay
Mean	7.4	12.0	4.3	3.7	

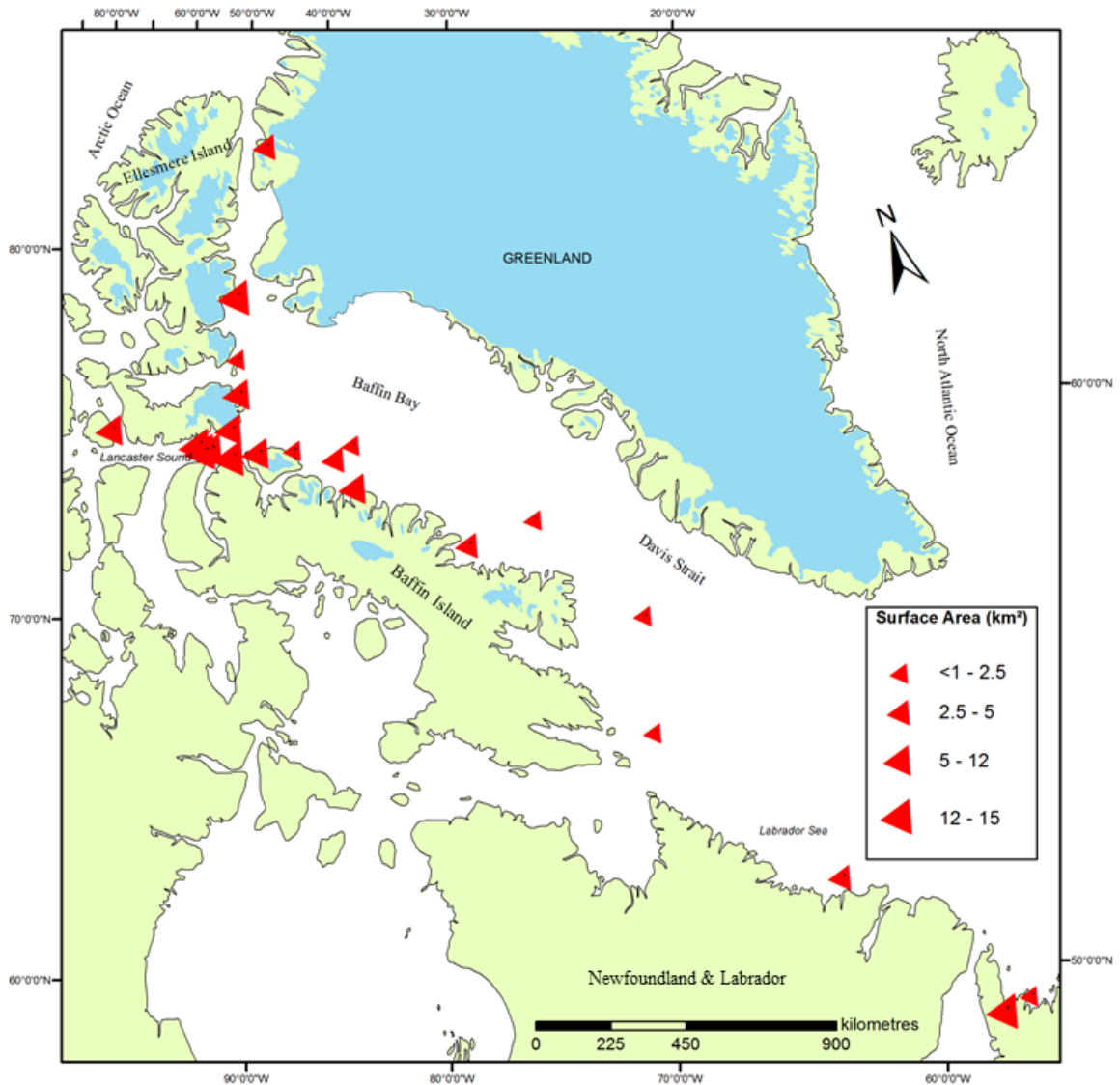


Figure 4.2: Distribution of the modelled ice islands. Surface area ranges are indicated by the graduated symbology. Glaciated regions are in blue.

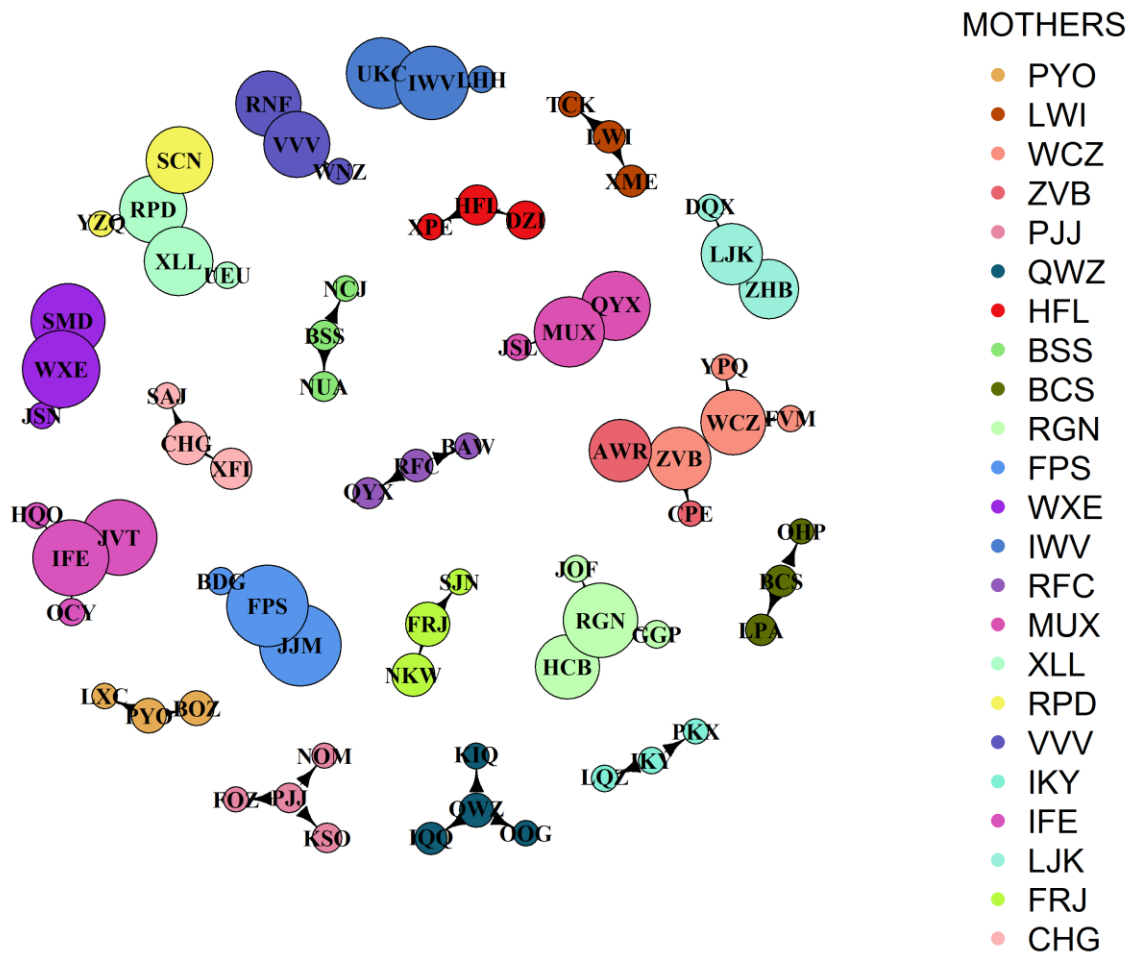


Figure 4.3: Network graph of the modelled ice islands represented by nodes (circles) and subsequently calved fragments (daughters) in matching colours. The ice island name is indicated by the text at the centre of the node and relative fragment size corresponds to node size. Some of the sketched ice islands are fragments of other modelled ice islands, as can be observed by the groupings of different mothers (e.g. RPD-RGN, WCZ-ZVB).

4.2 Sensitivity analysis results

Descriptive statistics of MPS in the peak stress zones (all elements located within a 60 m radius of the element that reaches the maximum of MPS) for each mesh resolution are summarized in **Table 4.2**. The deviations in mean, maximum and minimum MPS between element resolutions are also shown. **Figure 4.4** shows a plot of the differences in the maximum of MPS between each resolution and indicates an acceptable amount of

deviation between the resolution that was selected for use in this study (~20 x 20 x 10) and the finest modelled resolution of 10 x 10 x 10 (< 0.5% deviation between mean, maximum, and minimum results). The RMSE of the element which reached the maximum of MPS at a 20 x 20 x 10 resolution when compared to the finest resolution (10 x 10 x 10) was 284 Pa (stress range: 0.0 -147 kPa).

Table 4.2: Sensitivity analysis results. Descriptive statistics of MPS from the sensitivity analysis solutions at different element resolutions (kPa) (left) and deviations of the mean, maximum, and minimum principal stress of each resolution when compared to those of the finest resolution of elements (right).

Mesh (m)	Maximum Principal Stress (kPa)				Deviations from 10 m elements		
	Mean	St. Dev.	Max	Min	Δ Mean	Δ Max.	Δ Min.
10x10x10	13.1 \pm 0.1	20.9	147.3	-211	0.0	0.0	0.0
20x20x10	13 \pm 0.1	20.8	147.2	-211	-0.5	-0.1	0.3
20x20x20	13.6 \pm 0.2	20.5	126.6	-188	3.8	-14.1	-10.8
40x40x40	15.1 \pm 0.5	20.2	69.2	-119	15.6	-53.1	-43.7

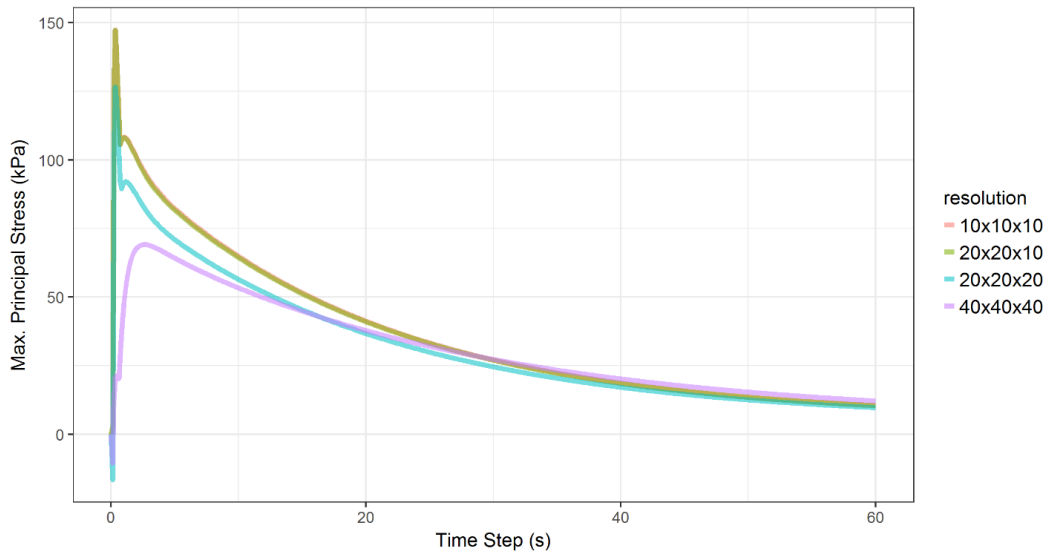


Figure 4.4: Time step history of the element which reaches the maximum of MPS at each state plotted for 4 different mesh resolutions. Precision of the model mesh resolution (20 x 20 x 10 m) follows the finest resolution (10 x 10 x 10 m) so well that they cannot be distinguished.

4.3 Uniform ram results

Ice islands with a uniform ram produced unrealistic stress distributions when compared to the corresponding post-calving remote sensing imagery in CI2D3 (calving plots). MPS in the model runs concentrated towards the centre of the bottom ice surface, and not towards the edges where calving actually took place. In cases where ice islands were particularly long, MPS peaked at opposite ends of the ice island in the beginning and coalesced at the centre later in the simulation (**Figure 4.5; b**). Multiple fractures formed in these peak stress regions and radiated outwards. This resulted in many lengthy fractures, however two fully independent fragments were never created (see for example [Appendix A](#)).

Seven of the 23 ice islands (30%) with a 20 m long uniform ram reached stresses that exceeded the flexural strength of ice chosen for this study (500 kPa). Maximum of MPS of modelled ice islands that did not fracture ranged from 407-487 kPa with a mean of 454

kPa. Four of the ice islands that reached failure were among the largest in the subset with surface areas ranging from 9.47 km² to 14.74 km². All modelled ice islands with a uniform ram of 40 and 60 m exceeded the flexural strength of ice.

4.4 Localized ram results

Ice islands modelled with localized rams developed fractures that generally matched break up patterns from the calving plots (e.g. **Figure 4.5; c**).

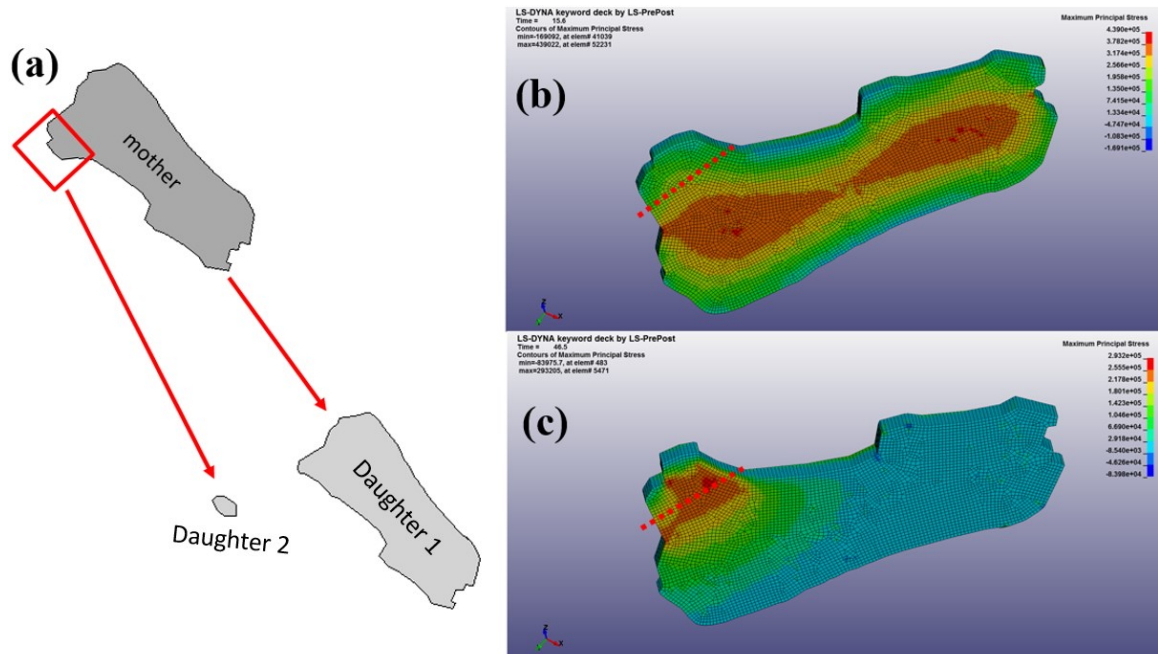


Figure 4.5: Comparison between a calving plot and FEA simulation results of ice island “20101106_113811_r2_12_LWI_40”. (a) shows a calving plot with a mother ice island and its associated daughter fragments following the calving event. (b) shows the results of an FEA simulation with a 40 m long uniform ram and (c) shows the results of a simulation with a 40 m long localized ram. Note that b and c are images of the bottom surface. The portion of the ice island assumed to calve is indicated by the red dashed lines. The distribution of high stresses from (c) were inferred to agree with the calving results of (a).

Of the modelled ice islands with localized rams, eight of the 23 ice islands (35%) with a 20 m long ram exceeded the flexural strength of ice in the model. For ice islands that did not fracture, the mean maximum MPS was 386 kPa, with a minimum maximum MPS of 283 kPa and a maximum maximum MPS of 494 kPa. All ice islands with 40 and 60 m long rams exceeded the flexural strength threshold of ice used in this study.

Although the location of initial peak stresses tended to match the calving locations assumed from the CI2D3 database, the fractures did not penetrate the uppermost layer of elements in the mesh (**Figure 4.6**). This prevented a smaller fragment from detaching from the larger fragment. Since neither piece was in a separate state of hydrostatic equilibrium (via elimination of the ram), stresses continued to build and radiate towards the rest of the ice island and cause additional unrealistic fractures to propagate. In spite of this model artifact, it was assumed that the model produced a realistic calving event 1) if the initial fracture penetrated most of the ice island thickness, and 2) that fracture length and orientation matched the calving edge from the calving plot (see for example Appendix B).

The length of the fractures produced by localized rams roughly matched the length of the ram extent of the ice island. In the few cases where the ice island calving edge was irregularly shaped, cracks would not follow this direction.

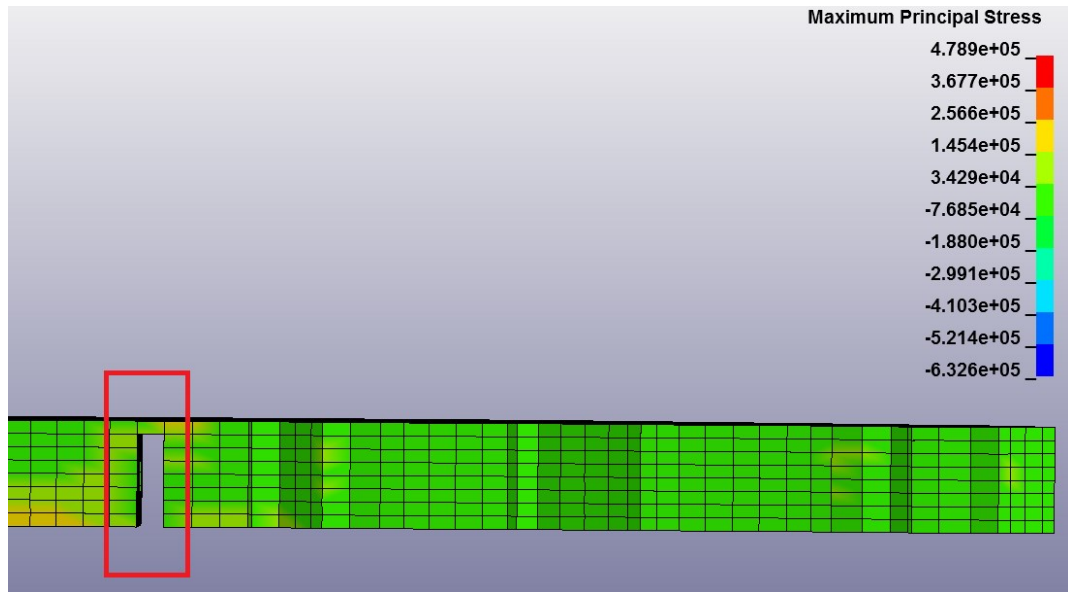


Figure 4.6: Ice island simulation showing failure for the topmost element layer to erode after the propagation of a fracture (red box).

4.5 Reduced localized ram extent results

The ice island volumes, ram volumes, and percentage of total volume occupied by the rams when outfitted with a localized ram (of half of its original extent) are shown in

Table 4.3.

Table 4.3: Volume and lengths of ice island and meshes with ram extents of half the original localized extent, with ram volume as a percentage of total volume.

Inst	Ice island		Length (m)	Ram		
	Volume (m ³)	Volume (m ³)		Extent (m)	% of total	Outcome
LWI	1.47E+08	6.69E+05	20	478	0.5	no calving
LWI	1.48E+08	1.33E+06	40	475	0.9	no calving
LWI	1.49E+08	1.76E+06	60	419	1.2	calving
PJJ	9.52E+07	4.49E+05	20	321	0.5	no calving
PJJ	9.59E+07	9.29E+05	40	332	1	calving
PJJ	9.71E+07	1.52E+06	60	361	1.6	calving
BSS	1.10E+08	7.05E+05	20	504	0.6	no calving
BSS	1.12E+08	1.57E+06	40	559	1.4	calving
BSS	1.13E+08	2.36E+06	60	561	2.1	calving
IKY	3.00E+07	3.17E+05	20	27	1.1	no calving
IKY	3.05E+07	6.17E+05	40	220	2	no calving
IKY	3.12E+07	9.76E+05	60	232	3.1	no calving
LJK	7.61E+08	3.09E+06	20	2210	0.4	calving
LJK	7.65E+08	6.18E+06	40	2210	0.8	calving
LJK	7.68E+08	9.22E+06	60	2200	1.2	calving
Mean	2.30E+08	2.11E+06		741	1.2	

Only one ice island with a 20 m ram of half its original extent reached the flexural strength threshold of ice. Mean maximum MPS was 274 kPa, with a range from 205 kPa to 407 kPa.

For ice islands with a 40 m long ram, two did not exceed the failure threshold of ice used in this study. Mean maximum MPS of these two modelled ice islands was 387 kPa (357 kPa and 417 kPa). Only one ice island with a 60 m long ram did not exceed the failure threshold (maximum MPS = 489 kPa).

The localized reduced extent rams induced fractures that matched the location of fractures indicated by the calving plots (see for example [Appendix C](#)), but with

comparatively longer ram lengths than those described in **Section 4.3**. **Table 4.4** shows an example of those differences for ram lengths of 20 m.

Table 4.4: Results of the maximum MPS of the five ice islands with a localized ram length of 20 m when its extent was shortened by half the original extent. Note that for “LJK”, the values come from the Limitless Flexural Strength analysis (**Section 3.9**), since its stresses exceeded the flexural strength limit used in this study.

Inst	100% Extent (kPa)	50% Extent (kPa)	Deviations (%)
LWI	347	205	-41
PJJ	547	417	-24
BSS	346	261	-25
IKY	283	215	-24
LJK	953	927	-3
Mean	495	411	23

4.6 Limitless flexural strength results

The total potential for MPS of ice islands with a localized ram and limitless flexural strength are shown in **Figure 4.7**. Mean maximum MPSs were 519, 902, and 1280 kPa for 20, 40, and 60 m long rams, respectively, indicating that stress increases roughly by 60-70% per 20 m extension of the ram in the length direction.

It was noted that one ice island with a particularly irregularly-shaped edge adjoined by a ram ("PYO") induced very large stresses (> 2 MPa with a ram length of 20 m).

Statistics of ice island dimensions, ram dimensions and total stress magnitude were taken from the ice islands from this experiment for statistical modelling: mean total ice volume, ram volume, and proportion of total volume occupied by the ram was $5.96 \times 10^8 \text{ m}^3$ (95% CI: $\pm 9.6 \times 10^7 \text{ m}^3$), $6.066 \times 10^6 \text{ m}^3$ (95% CI: $\pm 1.06 \times 10^6 \text{ m}^3$), and 0.02 % (95 % CI: ± 0.003), respectively.

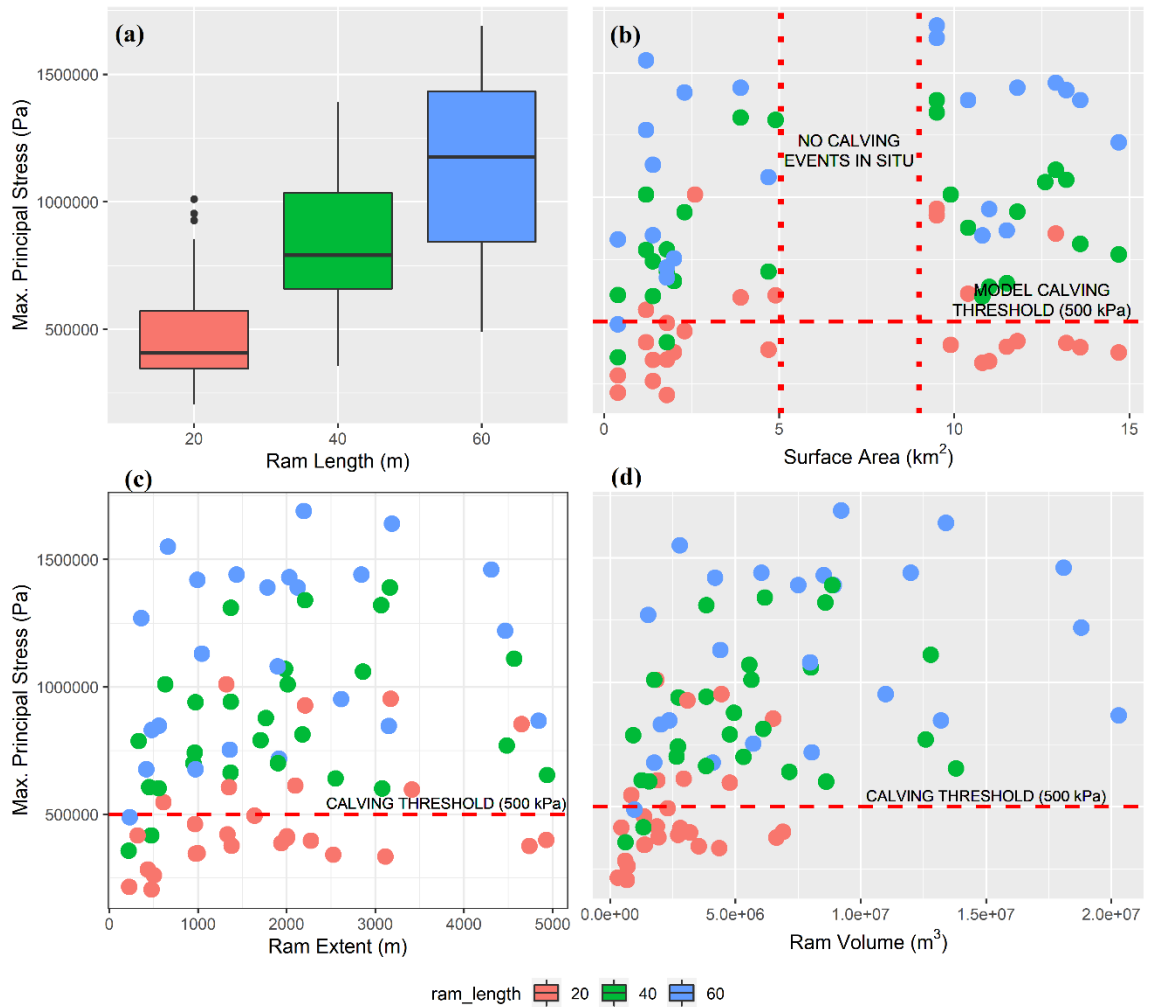


Figure 4.7: Various plots of MPS from the Limitless Flexural Strength analysis as a function of different ice island attributes (ram length (a), surface area (b), ram extent (c), and ram volume (d)). (b) indicates that there were no floating ice islands between 4.5 and 8.5 km² that calved in the field (as observed in CI2D3).

4.7 Empirical model results

All morphological variables were positively skewed (0.2-1.83) and total ice volume was bimodal (Table 4.5; Figure 4.8). Transformed variables, such as the square root of maximum stress (W : 0.97, p : 0.06), the logarithm of the percent of volume in the ram (W : 0.99, p : 0.93), the cube root of ram volume (W : 0.98, p : 0.38) and ram extent (W : 0.97, p : 0.04) were transformed to an acceptable degree of normality. Total ice volume (W : 0.87, p : 1.071×10^6) was used in the MLR, although it was not normally distributed.

Table 4.5: Skewness before and after transformation of ice island variables

Variable	Skew before	Skew after	Transformation
Stress	0.92	0.23	square root
Total volume	0.2	-0.04	square root
Ram volume	1.32	0.28	cube root
Ram width	0.78	-0.01	cube root
Ram % of volume	1.86	0.03	logarithm

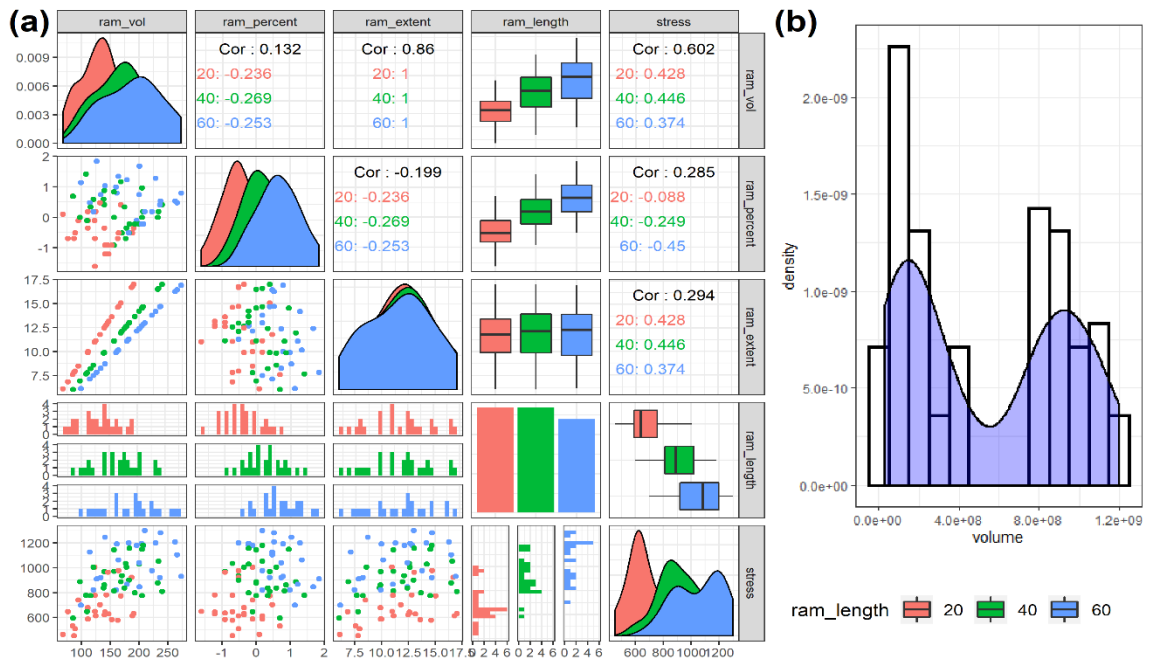


Figure 4.8: A scatterplot matrix of the transformed variables indicating moderate relationships between MPS and each of ram length and ram volume (a). The histogram shows the bimodal distribution of the raw volume data (b).

The VIF test indicated ram volume and the percentage of total ice volume contained within the ram were excessively multicollinear and were eliminated from the model. The pruned multiple regression model used to predict MPS indicated ram length ($p < 0.001$), the ram extent ($p < 0.01$), and the interaction term between ram percent and ram length ($p < 0.05$) were statistically significant variables. Model validation metrics extracted from the k-folds bootstrapped model were considered acceptable ($R^2 = 0.54$, RMSE = 20 kPa, MAE = 14 kPa). The original model had an $R^2 = 0.60$, which indicates a shrinkage of 0.065. The model coefficients, their 95% confidence interval, standard error, p-values and the percentage of total variation explained by the variable are shown in **Table 4.5**. Interaction terms between ram length and volume, ram extent and ram volume, and ram length and the percent of total ice volume within the ram were also statistically significant ($p = 0.004$, $p = 0.0003$, $p = 0.02$, respectively). The adjusted R^2 of the model was 0.6.

Table 4.6: Summary table of the multiple regression model and the percent of total variation explained by the model.

Predictors	Estimated	CI	St. error	p	% of variance
(intercept)	237.57	86.67 - 388.46	75.73	0.002	
Ram length	11.15	8.65 - 13.66	1.26	<0.001	48
Ram extent	18.52	7.58 - 29.47	5.49	0.001	9
ram length:ram %	-1.49	-2.80 - 0.18	0.66	0.027	3

From the results of the MLR, the magnitude of MPS can be modelled as:

$$\sigma_{max} = \sqrt{11.15r_l + 18.52\sqrt[3]{r_e} - 1.49 \log(r_p) r_l} \quad (4.1)$$

where σ_{max} is MPS, r_l is the length of the ram, r_e is the ram extent, and r_p is the percent of total volume contained within the ram.

The ram length and ram extent were statistically significant variables in the ANCOVA model (**Table 4.7; Table 4.8**). The interaction between total ice volume and ram extent ($p = 0.09$) and the percentage of total volume contained within the ram ($p = 0.106$) were not statistically significant at the 0.05 alpha threshold, but were included in the model since their removal significantly decreased model performance according to AIC and ANOVA tests.

The relative importance of the interaction term between total ice volume and ram extent may have been masked in the MLR due to the bimodal distribution total ice volume the change of slope between "low" and "high" categories. The bivariate regression model that predicts stress as a function of ice volume determined ice islands with low total ice volume to have a statistically significant positive relationship with stress ($p = 0.02$, $R^2 = 0.12$), but not with ice islands of high total ice volume ($p = 0.48$, $R^2 = 0.02$) (**Figure 4.9**).

Table 4.7: ANCOVA summary table. Ram length and ram extent were statistically significant, similar to the MLR model. The interaction between the ram extent and the volume and the percent of total volume contained within the ram were statistically significant in the ANCOVA, but not in the MLR model. The sum of squares (“Sum of sq.”), mean square error (“Mean sq.”), F-statistic (“F. value”), p-value (“PR(>5)”), and the percentage of total stress variance explained by the independent variable (“% of Variance”) are also shown, respectively. The bold indicates statistical significance at the < 0.001 alpha level.

Predictors	Df	Sum of sq.	Mean sq.	F. value	Pr (>5)	% of Variance
Ram length	2	1837935	918967	46.797	< 0.001	49.93
Ram extent	1	316934	316934	16.14	< 0.001	8.61
ram_extent:vol_fac	1	59778	59778	3.044	0.085297	1.62
Ram percent	1	52539	52539	2.676	0.106267	1.43
Residuals	72	1413873	19637			

Table 4.8: Linear model summary table for the ANCOVA model coefficients. The coefficients for 20 m long rams and low volumes are not shown because they are multiplied by the intercept coefficient. The estimated coefficients (“Estimated”), standard error (“St. error”), and p-values (“Pr(>5)”) are shown, respectively.

Predictors	Estimated	St. error	Pr (>5)
(intercept)	305.547	99.998	0.00315
ram_length40	301.305	46.885	< 0.001
ram_length60	480.651	59.617	< 0.001
ram_extent	32.797	9.59	0.00103
ram_percent	-96.256	40.282	0.01949
ram_extent:volfachhigh	-8.702	4.987	0.0853

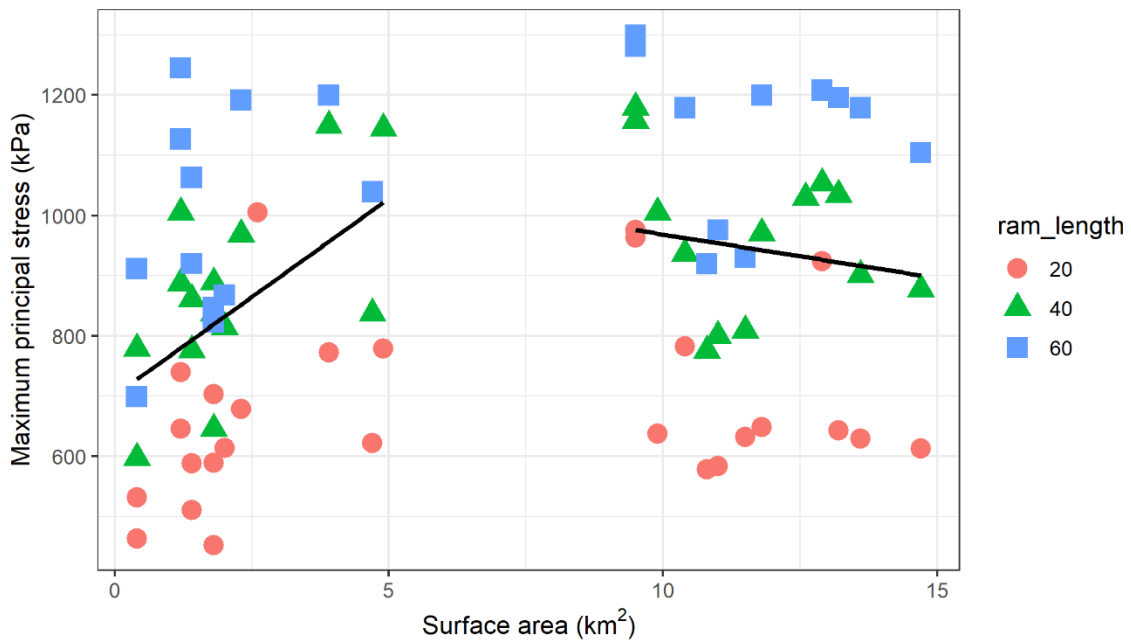


Figure 4.9: The maximum of MPS of each ice island with a regression line plotted through each separate nominal category of total ice volume (low and high total volume). Ice islands with low total ice volume have a statistically significant positive effect on MPS, but there is no statistically significant relationship in ice islands with high total ice volume.

5.0 Discussion

This study aimed to back analyze real ice island calving events by synthesizing rams of various dimensions to real ice island shapes. Exact dimensions of rams of the ice islands in this study remain unknown. In order to model the footloose mechanism in this sample of ice islands, assumptions of ram shapes and sizes were made. By doing this, the likelihood of different ram characteristics was assessed, which provides some framework for future fracture modelling until more field data of ram morphology becomes available. In spite of the paucity of quantitative ram data, the effect that ram buoyancy has on stress in icebergs has been modelled since the 1980s (**Section 2.6**). However, the Sazidy et al. (2019) model is the latest and most comprehensive iteration of these models to date and was therefore chosen for the analyses in this study. The fact that it can predict stresses in 3-D meant that previously unexplored elements of the footloose mechanism could be analyzed for the first time, such as stress distributions throughout real ice island shapes, and the effect that ram extent has on stress magnitude. Below, the significance of these analyses and more are summarized and assessed.

5.1 Ram morphology

5.1.1 Symmetrical rams

Ice islands modelled with symmetrical rams developed stress at the centre of the bottom surfaces. These results were broadly consistent with Diemand et al. (1987) (**Section 2.6**), which assumes the location of maximum stress is the midpoint between the iceberg edges. In this study, multiple cracks propagated at the central part of the bottom surfaces of this ice islands. However, the fractures did not cross the length of the ice island, and therefore could not be assumed to result in the creation of two independent ice island

fragments. Instead, fractures radiated outwards from the centre in multiple, irregular directions (often resembling a spider web-like pattern) (**Figure 5.1**). The failure of these simulated fractures to resemble the inferred fracture patterns on the ice islands suggest that uniform rams are an unlikely cause of the calving events observed in this study.

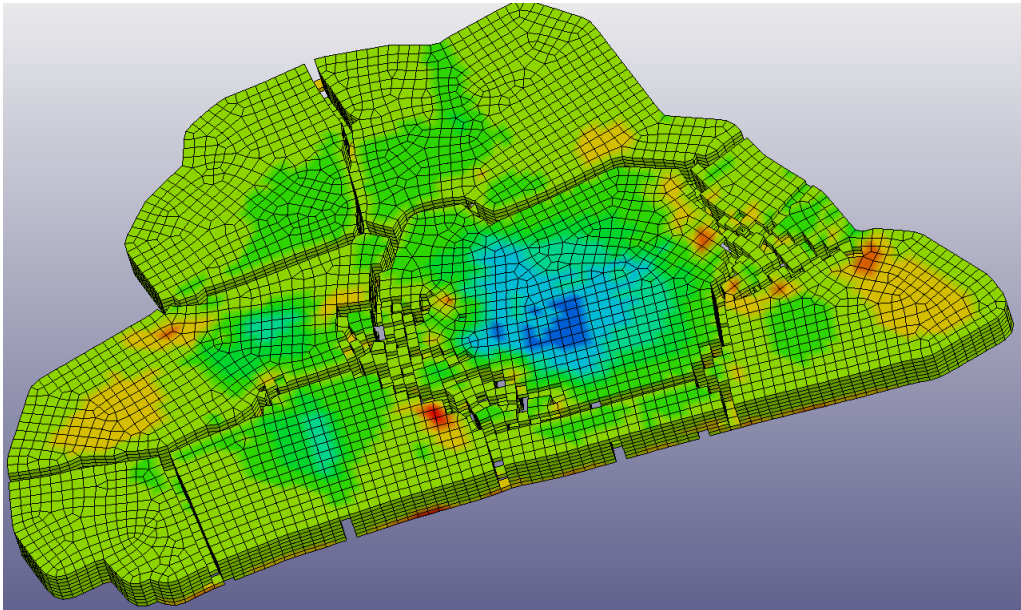


Figure 5.1: Fracture patterns on the bottom surface of ice island "20101203_115225_r2_4_PJJ" given a uniform ram of 40 m in length 27 s into the FEA results simulation. The resultant stress patterns were unrealistic and caused many irregularly oriented fractures to propagate throughout the ice island. Elements in green indicate low tensile stress, while red elements indicate higher stress.

Some possible explanations for the disparity between these results and the Diemand et al. (1987) model is that the former was designed for icebergs, which have a different (smaller) length to height ratio from that of ice islands and the greater surface areas of ice islands may prevent high stresses from reaching opposite ice island edges. The Diemand et al. (1987) model is also limited to a 2-D transect, and ignores the effect that a ram may have when attached to all sides of a 3-D ice island or iceberg, as opposed to flanking only opposite sides of a 2-D iceberg.

Further, the mean percentage of the calved ice island fragments (excluding the resultant larger mother) is 3.74% (**Table 4.1**), which indicates that the mechanism that caused these calving events tend to only remove a relatively small amount of mass from the ice island.

There is some evidence from the literature that perfectly uniform rams are unlikely to occur naturally. Stern et al. (2017) found that deterioration does not occur uniformly around ice islands due to different water column properties on opposite sides of grounded icebergs. Prior grounding events or other situations that may have led to an asymmetrical ram (prevailing wind and wave patterns local to the geographic positions of the ice islands) in the ice islands studied in this thesis may have led to differential erosion rates, but this information is not included in the CI2D3 database and is outside the scope of this study.

5.1.2 Localized rams

The localized ram experiment caused stresses to concentrate in locations that better matched the calving edge obtained from the CI2D3 database (calving plots). The location where failure first occurred was generally reasonable: fractures propagated along the bottom surface of the ice island where detachment occurred and extended in the upwards direction, with only the topmost layer of elements failing to erode from the mesh. This lack of complete separation, taken to be a model artifact, is discussed in further detail in **Section 5.5**.

The fact that the model accurately reproduces realistic calving events implies that the synthesized ram dimensions and location may have been similar to those of the actual ram of these ice islands. This suggests that ice islands in this study most likely had rams

localized to the edges adjoining the calving (**Objective 3**). In contrast, uniform rams were not likely to have caused the patterns of calving in this subset.

5.1.3 Effect of a reduced ram extent

The reduced localized ram extents (distance perpendicular to the ice edge) caused stresses of a lower magnitude in the ice islands, while at the same time retaining a realistic peak stress zone. Findings from Wagner et al. (2014) state that for ice islands of thickness $t = 80$ m, failure occurs when the ram length exceeds ~ 60 -80 m (**Figure 5.2**). Results from the localized ram experiment described in **Section 4.4** show that an ice island with a ram extent approximately equal to that of the length of the calved fragment failed when ram lengths were between 20-40 m. However, when the ram extent was reduced by half (**Section 4.5**), longer ram lengths were required to exceed the flexural strength threshold (40-60 m, versus 20-40 m) (**Table 4.3**), although not to the ram lengths reported by Wagner et al. (2014) (~ 80 m at $t = 80$ m). It is suspected that if the modelled ice island rams were reduced even further in extent, calving may occur in the FEA with ram lengths of 60-70 m. These results are supported by the MLR, which indicate that the ram extent is a statistically significant variable with the second strongest effect on stress magnitude (further described in **Section 5.4**). Ram extent is therefore an important factor in determining total stress magnitude and should be considered in further models given that simulations show a shorter ram length may be sufficient to induce calving if the ram extent is increased correspondingly.

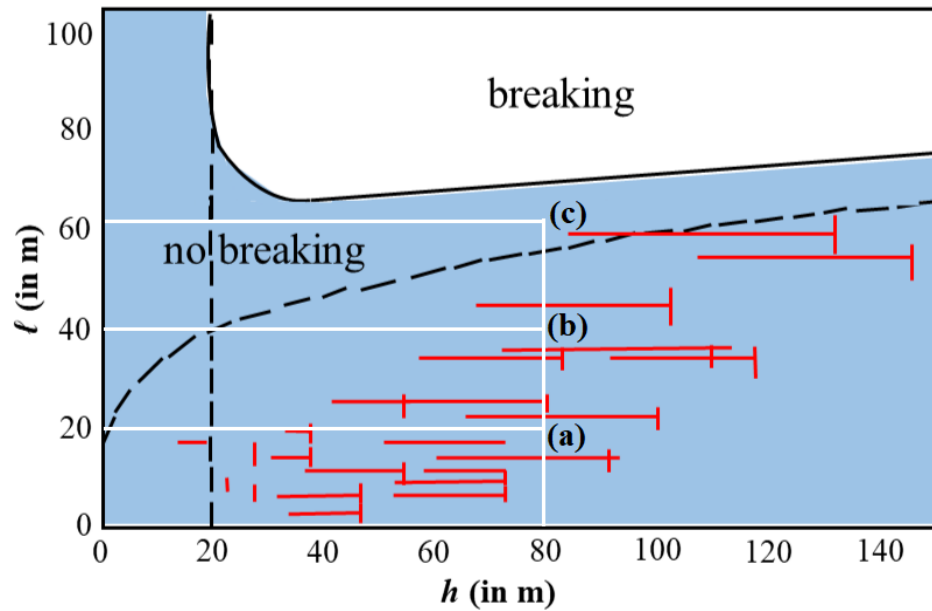


Figure 5.2: Regime of ice island thickness (h , x-axis) and ram length (l , y-axis) and whether or not a calving occurs (breaking/no breaking). The red lines indicate observational data of ram lengths from field data with error bars. The white lines indicate the thickness and ram lengths analyzed in this study: (a) 35% of ice islands with 20 m long localized rams fractured, and 100% of ice islands fractured with localized rams of 40 and 60 m (b & c). When considering the ice islands with localized rams of reduced extent, these figures are 32%, 93%, and 96%, respectively. It was found that calving occurred at much shorter ram lengths in the FEA (approximately equal to the length of the calved fragment), possibly due to the extent dimension that is not incorporated in previous models. Figure adapted from Wagner et al. (2014). The

5.2 Variations in flexural strength

Flexural strength of ice is reported to be highly variable from empirical studies (0.73 – 1.63 MPa) (Gagnon and Gammon, 1995). Ice samples selected for strength testing are generally free of fractures and impurities which otherwise lower the flexural strength considerably (Wagner et al. 2014). The physical size of ice samples collected for strength testing are also limited, and thus the scale effect of stress throughout fragments as large as ice islands are not well understood. The 500 kPa flexural strength threshold for this study was based on support from previous calving studies in the literature (Robe, 1980;

Vaughan, 1995), but this stress threshold was later removed to test the magnitude of MPS. For example, many modelled ice islands reached failure with rams that were as little as 20 m in length, but for some modelled ice islands to remain intact with ram lengths of 60 m (a possibility in the Wagner et al. (2014) model), the flexural strength would need to be increased to 700 kPa. This is a plausible limit based on empirical studies (Gagnon and Gammon, 1995).

5.3 Ice rheology

Ice was treated as a purely elastic material with a clearly defined flexural strength (500 kPa). The plastic nature of ice under high pressures was ignored since the ice thickness used in this study (80 m) was unlikely to cause significant deformation. Wagner et al. (2014) and Diemand et al. (1987) reported valid solutions with ice treated as an elastic material.

5.4 Statistical model parameters

Ram length was the single most important determinant of stress magnitude in the modelled ice island, accounting for 48% of the total variation of stress (**Table 4.6**). However, only three ram lengths were used in this study and intermediate-sized ram lengths (e.g. 10 and 30 m) should be explored to increase the prediction accuracy of the relationship between ram length and stress.

Ram extent was a statistically significant variable with a moderate effect on stress magnitude (9% of total variation in stress), which suggests that 3-D models of the footloose mechanism offer a justifiable benefit in model validity. Previous work by Wagner et al. (2014) and Diemand et al. (1987) have not explored ram extent in their

analytical models, and state that failures tend to occur with comparably longer ram lengths.

Total ice volume of drifting ice islands in this study was bimodal. The variable was transformed into a nominal variable of two levels (low and high total volume) which indicated that ice islands with low total ice volumes had a statistically significant and moderately positive effect on stress magnitude while high total ice volume had no statistically significant effect on stress. The change in slope between volume subsets (**Figure 4.9**) may be one reason that total volume (combined) was not detected as having a significant effect in the MLR, but was detected as an interaction in the ANCOVA mode.

However, the influence of volume may be suggested in the MLR from the statistical significance of the interaction between the percent of total ice volume contained in the ram and the ram length (3% of total stress variation); ice islands with higher ram volume to total ice volume ratios tend to tilt out of the water somewhat, which reduces the buildup of stress in the ice, whereas ice islands with lower ram volumes to total ice volumes will not tilt as much and therefore endure greater stress through bending (**Figure 5.3**). This is supported by the negative coefficient of the interaction term (**Table 4.6**).

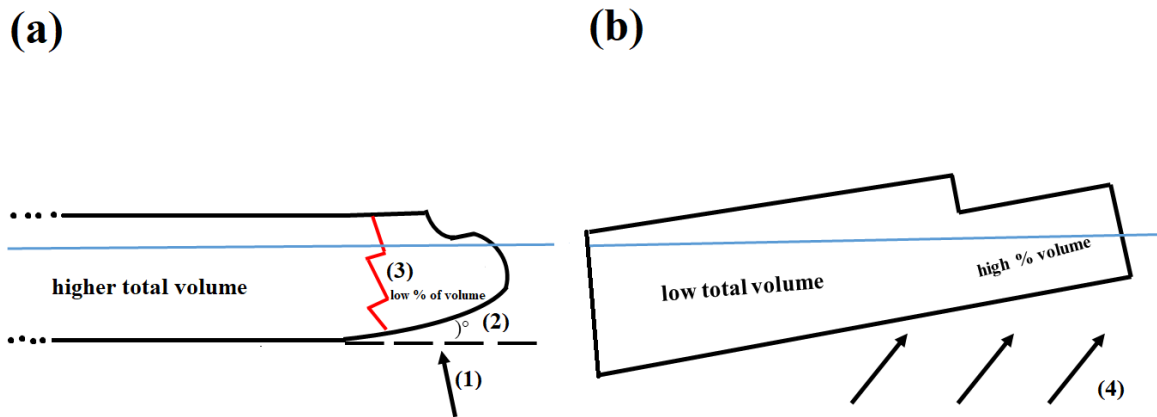


Figure 5.3: Schematic of an ice island torqueing (a) versus tilting (b). If the ice island has a comparatively smaller proportion of its total volume in the ram (a), the buoyant forces will cause bending/torqueing (1) that deflects the calving edge upwards (2). If the resultant stress is great enough, a fracture will occur at the location of maximum stress (3). However, when the total ice island volume is low compared to that of volume of the ram, the buoyant forces may instead cause the ice island to tilt out of the water, thereby avoiding stress buildup (4).

Further support for this effect is shown in the ANCOVA model, which preserved an interaction term between the ram extent and the total volume of ice with a negative coefficient. The percent of the total ice island volume contained in the ram was also statistically significant in the ANCOVA with a negative coefficient, which suggests diminishing increases in stress magnitude as the ram volume relative to total ice volume increases. Overall, the bootstrapped multiple regression model had a moderate performance ($R^2 = 0.54$), which suggests that large-scale fracture prediction is possible with these parameterizations.

5.5 Model limitations

This study revealed that the fractures simulated in the FEA model of ice islands with localized rams were often in good agreement with the location of fractures from the calving plots. However, the simulated fractures would not penetrate the topmost element

layer which prevented a complete separation of fragments, which also prevented these fragments from reaching a new state of hydrostatic equilibrium. The reason why this model artifact occurs is unclear at this time. However, it is likely a problem inherent to the element erosion method, which is an imperfect approach to simulating the behaviour of fractures through materials that are assumed to be homogenous (Unosson, 2005). The element erosion method in this model was used primarily as a means to easily identify the location where the failure threshold was first exceeded to determine if this simulated fracture zone was realistic. In order for the fragments to become separate, the flexural strength of the topmost layer of elements could be lowered, or alternate methods of simulating crack propagation could be explored. Lowering the flexural strength of the topmost element, for example, could be justified since the surfaces of ice islands tend to have fissures and melt ponds during the summer months, and are thus mechanically weaker than lower strata of ice (Wagner et al., 2014).

Central Processing Unit (CPU) processing times were a substantial limitation of this study. The 153 mesh permutations in this thesis took approximately four weeks of total processing time to complete. For example, ice islands with a surface area $> 9.5 \text{ km}^2$ took as much as 3 hours to be created using the automated ice island meshing program due to the hundreds of thousands of nodes and elements generated during the process.

Solution times ranged from a matter of minutes to hours, depending on the total volume of the mesh. Processing was lengthiest for the limitless flexural strength analysis since simulations were required to capture the maximum MPS (plateau) across the simulation (range 150 – 240 s) so that it could be used to produce the empirical models (MLR and ANCOVA; **Section 3.10**). However, the use of high performance computers or a

workflow that can exploit multiple cores would reduce both meshing and computing times.

Processing times also constrained the possible ram length and waterline height of the meshes. It was concluded that a mesh resolution of 20 x 20 x 10 m elements was the most ideal compromise between processing times and ram dimensions for the machine in use, but this limited ram lengths to increments of 20 m. Reducing the element resolution to 10 x 10 x 10 m elements (e.g. in order to simulate ram lengths of 10, 30, and 50 m) would result in unreasonably large computation times. A thickness of 80 m worked well with a mesh resolution of 20 x 20 x 10 m and allowed for the top of the ram to be located approximately at the waterline, which made the simulations realistic. This nominal thickness was also supported by the literature (Orheim, 1980) and *in situ* thickness estimates of a Petermann Ice Island (**Section 3.1**). Due to limited CPU power and mesh resolution and time constraints, further variations in thickness were considered outside the scope of this study.

Finally, it was not possible at the time of study to generate tabular results for MPS of elements across states (timesteps) with LS-DYNA. Future modelling endeavors with this software can be greatly expedited if this feature were included. Alternatively, other software that include this ability could be used for similar studies.

5.6 Future work

This study identified some of the characteristics and measurements of rams that can induce the calving of an ice island. However, due to the paucity of real ram data in the present time, more work should be done to build on these findings and produce more comprehensive models. Observation of ice islands from multi-beam, helicopter, or even

high-resolution optical imagery should be prioritized to corroborate all results in this study. Quantitative data of ice island ram dimensions are currently rare, and in the absence of these it is difficult to validate results from any footloose mechanism model. These measurements can also better guide knowledge gaps to address in new studies.

Thickness was an important variable of calving events in the Wagner et al. (2014) model, but it was not explored in this study due to time and processing constraints. Variations in thickness should be a central focus of future models to provide a more comprehensive overview of its effect on stress. This is especially important for modelling calving events of Antarctic ice islands, which can be over three to four times the thickness of Arctic ones.

This thesis also explored some of the effects of manipulating the ram extent (e.g. the reduced localized ram extent analysis), but these were limited in both scope and sample size. Future studies should examine how the variability of ram extent influences stress magnitude. For example, how calved fragments are affected by ram extents that are double the length of the calving edge, and if there is a minimum ram extent that can still produce a calving event.

It was noted during the limitless flexural strength experiment that rams adjoining a highly irregularly shaped ice island edge (“20100805_160926_es_2_PYO”) seemed to cause particularly high stresses and required more time for these stresses to plateau than other ice islands of a similar size (**Figure 5.4**). Though ice islands are generally characterized by relatively tabular shapes, highly irregular edges do sometimes occur naturally and the effect they have on calving should be explored further to confirm this.

Finally, the ice island observations in this study were made within weeks of calving events, and their morphologies at the time of modelling were presumed to play an important role in calving. Future studies should examine the effect rams have on prior morphologies of ice islands leading up to a calving. The absence of calving events in these "younger" versions of ice islands could help identify ice island morphologies that are conducive to break up.

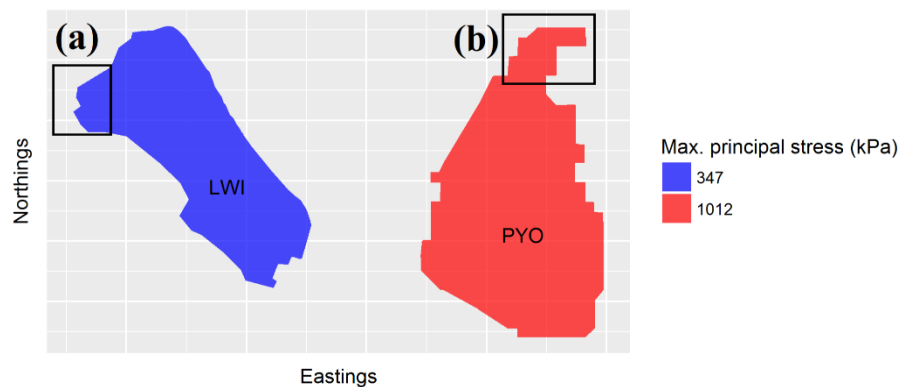


Figure 5.4: Polygons of ice island instances "20101106_113811_r2_12_LWI" and "20100805_160926_es_2_PYO" shaded according to their predicted absolute MPS when outfitted with a ram length of 20 m. The black squares (a & b) indicate the regions where rams were localized. "LWI" had a particularly rectangular edge and retained a low maximum MPS while "PYO" had among the most irregular calving edge and a predicted maximum MPS in excess of 1,000,000 kPa.

6.0 Conclusion

In situ studies of ice islands are exceedingly difficult to manage logistically due to the expense, remoteness and planning that it takes to visit them. There are dangers inherent in working on or near ice islands since their breakup is unpredictable, making it challenging to observe this ephemeral process as it unfolds. The release of the CI2D3 database now makes it easier to analyze the drift and areal deterioration of many individual ice islands across a fine temporal and spatial scale (Crawford et al. 2018) and use some of the calving event aftermaths it captured for modelling. This thesis determined the shape and dimensions of hypothetical rams that could simulate some of these calving events. Since the underwater dimensions of these ice islands were unknown, determination of accurate ram sizes was done in a step-wise manner by examining the effect that various ram shapes (uniform or localized), lengths, and extents had on stress distribution and magnitude.

The first objective (**Objective 1**) of this thesis was to examine the characteristics of ice islands in the field. This information was helpful to parameterize the FEA model that was run on ice islands selected from the CI2D3 database to meet the remaining objectives of this thesis. FEA was used to investigate break-up in the case of rams of a consistent length uniformly surrounding the perimeter of each ice island (**Objective 2**). The next experiment, which met **Objective 3**, was to model break-up caused by rams isolated to only edges that broke away during observed calving events (the calving edge). In conducting model runs for **Objective 3**, along with supplementary runs with a reduced ram extent, the length and extent of rams that caused calving were noted, thereby meeting the objective to determine what ram size is required to produce a calving event

(Objective 4). Finally, the flexural strength threshold of ice was removed from the model in order to determine the total stress magnitude of each of the ice island simulations.

These values were used to build a predictive model so that peak stresses could be predicted based on ram and ice island dimensions **(Objective 5).**

The main conclusions that follow from these five objectives are:

1. From 1080 radar traces over a ~ 4.5 km transect on one ice island (PII-A-1-f) along with a literature review of 3 papers (Forrest et al., 2012; Halliday et al., 2012; Rignot and Steffen, 2008), a thickness of 80 m was determined to be representative of ice islands within the study area. This information was used to parameterize the FEA model employed in the remainder of the study;
2. Rams are unlikely to surround the perimeter of ice islands uniformly. This type of ram configuration causes many unpredictable fractures that do not match the aftermath of the calving events shown in the images of the 23 selected ice islands;
3. For the 23 ice islands used in this study the rams most likely adjoin certain corners or edges of ice islands since, in the FEA simulations, this fringe demarcated, approximately, the outer extent of the future calved fragment;
4. The length of the ram needed to induce calving is highly dependent on the flexural strength of ice, but 93% and 96% of all the simulated ice islands (full and shortened ram extents) calved with ram lengths of 40 and 60 m, respectively;
5. Empirical relationships between ice island dimensions, ram dimensions, and stress magnitude exist such that stress can be predicted. The length of the ram is the most important factor in driving a footloose-style calving event, while the extent and the ratio of ram volume to total ice island volume play ancillary roles.

It was found that the calving events simulated in this thesis occurred with ram lengths shorter than those cited in previous footloose calving models. For example, Wagner et al. (2014) found that for an ice island of 80 m in thickness, a ram length of approximately 60–70 m is needed to induce calving. However, in the FEA, nearly all ice islands (96%) reached calving events with ram lengths <60 m, and many of these failed with lengths as little as 20 m. Since both studies adopted the same flexural strength threshold, this is thought to be attributed to the fact that Wagner et al. (2014) used a 2-D model, which ignores the stresses that are associated with ice island planar shape and ram extent. This study determined the extent of the ram to be an important ancillary factor in ice island calving, which likely reduces the length needed to cause calving when it is accounted for in a model. If footloose-type calving can occur at shorter ram lengths than assumed up to now (e.g. Wagner et al., 2014), this implies that this process is likely more common and therefore more important for ice island/iceberg deterioration than previously understood. However, few *in situ* measurements of rams exist to confirm this. At the present time, the only known ram length ever recorded in the literature was one of ~19 m on ice island "PII-B-1" in July 2012 days before it calved (Wagner et al., 2014). The fact that the ram attached to PII-B-1 was less than the maximum ram lengths determined in this study (~60 m), but still within a range that could possibly simulate calving (~20 m) supports that calving is possible at ram lengths shorter than previously thought.

Analyses of large-scale deterioration or calving events is still quite limited (Diemand et al., 1987; Scambos et al., 2005; Wagner et al., 2014; Sazidy et al., 2019). Despite the exploratory nature of this study, it has identified some of the factors that promote calving events when ice islands are adjoined by a ram below the water surface, and has provided

a foundation for further investigation into these factors. Further research steps that were considered in Chapter 4 are prioritized in the following. Addressing these knowledge gaps will help to provide more comprehensive and robust models for understanding the processes associated with ice island calving.

1. Future studies should be conducted with known *in situ* data of ram dimensions. This would help corroborate the findings discussed in this study. For example, that uniform rams are unlikely to exist in nature, or that ram lengths seldom exceed 60 m before calving occurs;
2. Variations in thickness should be explored in future 3-D models. Wagner et al. (2014) indicated that thickness plays a role in stress magnitude, so further examination will provide insight into the calving of ice islands with thicknesses observed in both the Arctic and the Antarctic (i.e., from 40 to 400 m in thickness (Halliday et al., 2012; Kristensen, 1983));
3. The effect of ram extent on stress should be evaluated further. This thesis showed that ram extent had an effect on stress magnitude and distribution, but further effort should be made to vary the extent of rams in future modelling studies to fully elucidate how this variable influences calving;
4. Ice island shape should be investigated as a factor in footloose-style calving events. Rams simulated along an irregularly-shaped ice island edge in this subset induced particularly high stresses and this should be confirmed by modelling more ice islands with such shapes adjoined by a ram;
5. This thesis confirms it is possible to reproduce footloose-style calving events with FEA; however, to ensure the model works well, it should also correctly predict

that ice islands will not calve if they did not actually do so in the field. Further modelling of the progression from this stable state to the one that ultimately calved will lead to a better understanding of the role of edge-wasting and simulated ram development as ice islands evolve over time.

As sea ice extent in the Arctic Ocean reduces due to climate warming, it is expected that an increase in ship traffic and offshore oil operations will result, underscoring the need to better constrain the risk that ice hazards, such as ice islands pose. Understanding the processes by which ice islands calve is an important addition to iceberg deterioration research, which can inform the management of marine hazards. Since drift trajectory models must incorporate deterioration rates to determine iceberg/ice island waterline length and mass, this understanding, via a robust deterioration model, can also be used to enhance the drift models which are in operational use. Such a model may help to avoid a future environmentally disastrous encounter between an iceberg and an offshore oil platform or a shipment of hazardous materials.

7.0 References

- Abaqus, 2017. How do mesh elements correspond to Abaqus elements? Accessed on October 22 2019. <https://abaqus-docs.mit.edu/2017/English/SIMACAECAERefMap/simacae-c-mgnconcelemcorresp.htm>.
- Althoff, W., 2017. The military importance and use of ice islands during the cold war, in: Luke Copland, Derek Mueller (Eds.), *Arctic Ice Shelves and Ice Islands*. Springer, Dordrecht, Netherlands, 343–366.
- Autodesk, 2019. Finite Element Analysis. Autodesk. Accessed on October 22 2019. <https://www.autodesk.ca/en/solutions/finite-element-analysis>.
- Bailey, E., Phillips, R., 2018. Iceberg risk to marginal field developments: physical tests to investigate free-floating iceberg contact with pipeline laid on the seabed. Presented at the Offshore Technology Conference, Houston, Texas.
- Ballicater Consulting Ltd., 2012. Ice Island and Iceberg Studies 2012. Contract Report No. 12-01. Canadian Ice Service, Environment Canada, Ottawa, Canada.
- Bathe, K.-J., 2014. *Finite Element Procedures*, 2nd ed. Prentice-Hall, Englewood Cliffs, N.J.
- Belkin, I., Kessel, S., 2017. Russian drifting stations on Arctic ice islands, in: Copland, L., Derek Mueller (Eds.), *Arctic Ice Shelves and Ice Islands*. Springer, Dordrecht, Netherlands, 367–394.
- Bell, T., Brown, T. (Eds.), 2018. *From Science to Policy in the Eastern Canadian Arctic: An Integrated Regional Impact Study (IRIS) of Climate Change and Moderization*. ArcticNet, Quebec City, QC.
- Benn, D.I., Cowton, T., Todd, J., Luckman, A., 2017. Glacier Calving in Greenland. *Current Climate Change Reports* 3, 282–290. <https://doi.org/10.1007/s40641-017-0070-1>.
- Bennett, R., Campbell, D.C., Furze, M.F.A., 2013. The shallow stratigraphy and geohazards of the northern Baffin Island shelf: studies to 2012. *Bulletin of Canadian Petroleum Geology* 62, 217–231. <https://doi.org/10.4095/292614>.
- Bevis, M., Harig, C., Khan, S.A., Brown, A., Simons, F.J., Willis, M., Fettweis, X., van den Broeke, M.R., Madsen, F.B., Kendrick, E., Caccamise, D.J., van Dam, T., Knudsen, P., Nylén, T., 2019. Accelerating changes in ice mass within Greenland, and the ice sheet's sensitivity to atmospheric forcing. *Proceedings of the National Academy of Sciences of the United States of America* 116, 1934–1939. <https://doi.org/10.1073/pnas.1806562116>.

- Bigg, G.R., Wei, H.L., Wilton, D.J., Zhao, Y., Billings, S.A., Hanna, E., Kadiramanathan, V., 2014. A century of variation in the dependence of Greenland iceberg calving on ice sheet surface mass balance and regional climate change. *Proceedings of the Royal Society A: Mathematical, Physical and Engineering Sciences* 470, 20130662–20130662. <https://doi.org/10.1098/rspa.2013.0662>.
- Budd, W.F., Jacka, T.H., 1989. A review of ice rheology for ice sheet modelling. *Cold Regions Science and Technology* 16, 107–144. [https://doi.org/10.1016/0165-232X\(89\)90014-1](https://doi.org/10.1016/0165-232X(89)90014-1).
- Burkardt, J., 2011. ISC 5939: Meshing for the Finite Element Method, lecture slides [PowerPoint presentation]. Accessed on October 11 2019. https://people.sc.fsu.edu/~jburkardt/classes/fem_2011/fem_meshing.pdf.
- Canadian Ice Service, 2005. MANICE: Manual of Standard Procedures for Observing and Reporting Ice Conditions. Environment Canada, Downsview, Ontario.
- Copland, L., Mortimer, C., White, A., McCallum, M., Mueller, D., 2017. Factors contributing to recent Arctic ice shelf losses, in: Copland, L., Derek Mueller (Eds.), *Arctic Ice Shelves and Ice Islands*. Springer, Dordrecht, Netherlands, 263–286.
- Copland, L., Mueller, D.R., Weir, L., 2007. Rapid loss of the Ayles Ice Shelf, Ellesmere Island, Canada. *Geophysical Research Letters*. 34, 6 pp. <https://doi.org/10.1029/2007GL031809>.
- Crawford, A., 2018. Ice island deterioration (Doctoral Thesis). Carleton University, Ottawa, Ontario. <https://doi.org/10.22215/etd/2018-13178>.
- Crawford, A., 2013. Ice island deterioration in the Canadian Arctic: rates, patterns and model evaluation (Master of Science Thesis). Carleton University, Ottawa, Ontario. <https://doi.org/10.22215/etd/2013-10024>.
- Crawford, A., Crocker, G., Mueller, D., Desjardins, L., Saper, R., Carrieres, T., 2018a. The Canadian Ice Island Drift, Deterioration and Detection (CI2D3) Database. *Journal of Glaciology* 64, 517–521. <https://doi.org/10.1017/jog.2018.36>.
- Crawford, A., Mueller, D., Desjardins, L., Myers, P.G., 2018b. The aftermath of Petermann Glacier calving events (2008-2012): ice island size distributions and meltwater dispersal. *Journal of Geophysical Research: Oceans* 123, 8812–8827. <https://doi.org/10.1029/2018JC014388>.

- Crawford, A., Mueller, D., Joyal, G., 2018c. Surveying Drifting Icebergs and Ice Islands: Deterioration Detection and Mass Estimation with Aerial Photogrammetry and Laser Scanning. *Remote Sensing* 10, 26 pp. <https://doi.org/10.3390/rs10040575>.
- Crawford, A., Mueller, D.R., Humphreys, E.R., Carrieres, T., Tran, H., 2015. Surface ablation model evaluation on a drifting ice island in the Canadian Arctic. *Cold Regions Science and Technology* 110, 170–182. <https://doi.org/10.1016/j.coldregions.2014.11.011>.
- Crawford, A., Wadhams, P., Wagner, T., Stern, A., Abrahamsen, P., Church, I., Bates, R., Nicholls, K., 2016. Journey of an Arctic ice island. *Oceanography* 29, 254–263. <https://doi.org/10.5670/oceanog.2016.30>.
- Crawley, M., 2007. *The R Book*. Wiley, Chichester, West Sussex, United Kingdom.
- Cuffey, K. M., & Paterson, W. S. B. 2010. *The physics of glaciers*. Burlington, MA: Butterworth-Heinemann/Elsevier.
- Davis, L., n.d. *Body Physics: Motion to Metabolism*. Accessed July 18, 2019. <https://openoregon.pressbooks.pub/bodyphysics/>.
- Dawson, J., Pizzolato, L., Howell, S.E.L., Copland, L., Johnston, M.E., 2018. Temporal and spatial patterns of ship traffic in the Canadian Arctic from 1990 to 2015. *Arctic* 71, 15–26. <https://doi.org/10.14430/arctic4698>.
- Derksen, C., Smith, S.L., Sharp, M., Brown, L., Howell, S., Copland, L., Mueller, D.R., Gauthier, Y., Fletcher, C.G., Tivy, A., Bernier, M., Bourgeois, J., Brown, R., Burn, C.R., Duguay, C., Kushner, P., Langlois, A., Lewkowicz, A.G., Royer, A., Walker, A., 2012. Variability and change in the Canadian cryosphere. *Climatic Change* 115, 59–88. <https://doi.org/10.1007/s10584-012-0470-0>.
- Diemand D., Nixon, WA., Lever JH., 1987. On the splitting of icebergs - natural and induced. *Proceedings of the 6th International Offshore Mechanics and Arctic Engineering Symposium*. America Society of Mechanical Engineers, Houston, Texas, USA, 379-385.
- Dowdeswell, J., Jeffries, M.O., 2017. Arctic ice shelves: an introduction, in: Copland, L., Derek Mueller (Eds.), *Arctic Ice Shelves and Ice Islands*. Springer, Dordrecht, Netherlands, 3–21.
- Duval, P., Montagnat, M., Grennerat, F., Weiss, J., Meyssonier, J., Philip, A., 2010. Creep and plasticity of glacier ice: a material science perspective. *Journal of Glaciology* 56, 1059–1068. <https://doi.org/10.3189/002214311796406185>.

- Eik, K., Gudmestad, O.T., 2010. Iceberg management and impact on design of offshore structures. *Cold Regions Science and Technology* 63, 15–28. <https://doi.org/10.1016/j.coldregions.2010.04.008>.
- Environment and Climate Change Canada, 2019. Canada's Changing Climate Report. Ottawa, Canada. https://www.nrcan.gc.ca/sites/www.nrcan.gc.ca/files/energy/Climate-change/pdf/CCCR_FULLREPORT-EN-FINAL.pdf.
- Fagan, M., 1992. *Finite Element Analysis*. Longman Group UK.
- Fastook, J.L., Schmidt, W.F., 1982. Finite Element Analysis of calving from ice fronts. *Annals of Glaciology* 3, 103–106. <https://doi.org/10.3189/S0260305500002603>.
- Flynn, M., 2013. Ice scour risk and protection on the Grand Banks. *Journal of Undergraduate Engineering Research and Scholarship* 6 pp.
- Forrest, A., Hamilton, A.K., Schmidt, V., Laval, B., Mueller, D., Crawford, A., Brucker, S., Hamilton, T., 2012. Digital terrain mapping of Petermann Ice Island fragments Canadian High Arctic. *Proceedings of the 21st International Symposium on Ice*. Dalin, China.
- Fuglem, M., Jordaan, I., 2017. Risk analysis and hazards of ice islands, in: Copland, L., Derek Mueller (Eds.), *Arctic Ice Shelves and Ice Islands*. Springer, Dordrecht, Netherlands, 395–415.
- Gagliardini, O., 2011. Anisotropic ice flow, in: Singh, V.P., Singh, P., Haritashya, U.K. (Eds.), *Encyclopedia of Snow, Ice and Glaciers*. Springer Netherlands, Dordrecht, 44–54. https://doi.org/10.1007/978-90-481-2642-2_658.
- Gagnon, R.E., Gammon, P.H., 1995. Characterization and flexural strength of iceberg and glacier ice. *Journal of Glaciology* 41, 103–111. <https://doi.org/10.3189/S0022143000017809>.
- Geuzaine, C., Remacle, J.-F., 2019. *Gmsh reference manual*. Accessed on October 11 2019. <http://gmsh.info/doc/texinfo/gmsh.pdf>.
- Glen, J.W., Perutz, M.F., 1955. The creep of polycrystalline ice. *Royal Society* 228. <https://doi.org/10.1098/rspa.1955.0066>.
- Gold, L.W., 1977. Engineering properties of fresh-water ice. *Journal of Glaciology* 19, 197–212. <https://doi.org/10.3189/S00221430000215608>.
- Greaves, G.N., 2013. Poisson's ratio over two centuries: challenging hypotheses. *Notes and Records of the Royal Society Journal of the History of Science* 67, 37–58. <https://doi.org/10.1098/rsnr.2012.0021>.

- Halliday, J., King, T., Pradeep, B., Copland, L., Mueller, D., 2012. Petermann ice island “A” survey results, offshore Labrador. Proceedings of the Offshore Technology Conference. Houston, Texas, 14 pp.
- Hanson, B., Hooke, R., 2000. Glacier calving: a numerical model of forces in the calving-speed/water-depth relation. *Journal of Glaciology* 46, 188–196. <https://doi.org/10.3189/172756500781832792>.
- Hattersley-Smith, G., 1962. The term “ice island.” *Journal of Glaciology* 4, 131.
- Heath, T., 1897. On Floating Bodies, in: *The Works of Archimedes*. Cambridge University Press, Cambridge, 524 pp.
- Hill, B.T., 2010. Ship collision with iceberg database. No. TR-2005-17. National Research Council.
- Holland, I., 1974. Fundamentals of the finite element method. *Computers and Structures* 4, 3–15.
- Iken, A., 1977. Movement of a large ice mass before breaking off. *Journal of Glaciology* 19, 595–605. <https://doi.org/10.3189/S0022143000215505>.
- Jansen, D., Sandhäger, H., Rack, W., 2005. Model experiments on large tabular iceberg evolution: ablation and strain thinning. *Journal of Glaciology* 51, 363–372. <https://doi.org/10.3189/172756505781829313>.
- Jawak, S.D., Bidawe, T.G., Luis, A.J., 2015. A review on applications of imaging synthetic aperture radar with a special focus on cryospheric studies. *Advances in Remote Sensing* 04, 163–175. <https://doi.org/10.4236/ars.2015.42014>.
- Joint Technical Commission for Oceanography and Marine Meteorology, 2015. Sea Ice Nomenclature. Accessed on October 10 2019. https://www.jcomm.info/index.php?option=com_oe&task=viewDocumentRecord&docID=14598.
- Jeffries MO., 2002. Ellesmere Island ice shelves and ice islands. Williams RS and Ferrigno JG (Eds.), *Satellite Image Atlas of Glaciers of the World: North America*. United States Geological Survey, Washington, J147–J164.
- Jeffries, M.O., 1992. Arctic ice shelves and ice islands: origin, growth and disintegration, physical characteristics, structural-stratigraphic variability, and dynamics. *Reviews of Geophysics* 30, 245–267. <https://doi.org/10.1029/92RG00956>.

- Jeffries, M.O., Sackinger, W., 1990. Near-real-time synthetic aperture radar detection of a calving event at the Milne ice shelf, NWT, and the contribution of offshore winds. Proceedings of the Second International Conference on Ice Technology., Computational Mechanics Publications, Southampton, 321–331.
- Jeffries, M.O., Sackinger, W.M., 1989. Airborne SAR characteristics of arctic ice shelves and multiyear landfast sea ice, and the detection of massive ice calvings and ice islands, in: 12th Canadian Symposium on Remote Sensing Geoscience and Remote Sensing Symposium. pp. 2715–2718.
<https://doi.org/10.1109/IGARSS.1989.577973>.
- Klein, C.A., Cardinale, G.F., 1993. Young's modulus and Poisson's ratio of CVD diamond. *Diamond and Related Materials* 2, 918–923.
- Knowles, N.C., 1984. Finite element analysis. *Computer-Aided Design* 16, 134–140.
- Koenig, L.S., Greenaway, K.R., Dunbar, M., Hattersley-Smith, G., 1952. Arctic ice islands. *Arctic* 5, 67–103.
- Krajick, K., 2001. Tracking icebergs for clues to climate change. *Science* 292, 2244–2255. <https://doi.org/10.1126/science.292.5525.2244>.
- Kristensen, M., 1983. Iceberg calving and deterioration in Antarctica. *Progress in Physical Geography: Earth and Environment* 7, 313–328.
<https://doi.org/10.1177/030913338300700301>.
- Kubat, I., Sayed, M., Savage, S.B., Carrieres, T., Crocker, G., 2007. An operational iceberg deterioration model. Proceedings of the Sixteenth International Offshore and Polar Engineering Conference. Lisbon, Portugal, 652–657.
- Lim, H., Hoag, S., 2013. Plasticizer effects on physical–mechanical properties of solvent cast Soluplus® films. *American Association of Pharmaceutical Scientists PharmSciTech* 14, 903–910. <https://doi.org/10.1208/s12249-013-9971-z>.
- Long, J.T., Neogi, S., Caldwell, C.M., DeLange, M.P., 2018. Variation inflation factor-based regression modeling of anthropometric measures and temporal-spatial performance: Modeling approach and implications for clinical utility. *Clinical Biomechanics* 51, 51–57. <https://doi.org/10.1016/j.clinbiomech.2017.11.008>.
- LS DYNA, 2007. LS DYNA Keyword User's Manual. Accessed on October 11 2019.
https://www.dynasupport.com/manuals/ls-dyna-manuals/ls-dyna_manual_volume_i_r11.pdf.
- LS DYNA, n.d. Mass Scaling. Accessed on October 11 2019.
<https://www.dynasupport.com/howtos/general/mass-scaling>.

- Mandal, T., Edil, T.B., Tinjum, J.M., 2018. Study on flexural strength, modulus, and fatigue cracking of cementitiously stabilised materials. *Road Materials and Pavement Design* 19, 1546–1562. <https://doi.org/10.1080/14680629.2017.1325772>.
- Mobasher, M.E., Duddu, R., Bassis, J.N., Waisman, H., 2016. Modeling hydraulic fracture of glaciers using continuum damage mechanics. *Journal of Glaciology* 62, 794–804. <https://doi.org/10.1017/jog.2016.68>.
- Mueller, D., Copland, L., Jeffries, M.O., 2017. Changes in Canadian arctic ice shelf extent since 1906, in: Copland, L., Derek Mueller (Eds.), *Arctic Ice Shelves and Ice Islands*. Springer, Dordrecht, Netherlands, 109–148.
- Mueller, D., Crawford, A., Copland, L., Van Wychen, W., 2013. Ice Island and Iceberg Fluxes from Canadian high Arctic Sources. Report to the Northern Transportation Assessment Initiative. Innovation Policy Group of Transport Canada, Ottawa, Canada.
- Mueller, D.R., Vincent, W.F., Jeffries, M.O., 2003. Break-up of the largest Arctic ice shelf and associated loss of an epishelf lake. *Geophysical Research Letters*. 30. <https://doi.org/10.1029/2003GL017931>.
- Nacke, M., 2016. Characterization of the coastal marine environment in the vicinity of a grounded iceberg, Canadian Arctic Archipelago (Master of Science Thesis). Carleton University, Ottawa, Ontario. <https://doi.org/10.22215/etd/2016-11365>.
- Nikishkov, G.P., 2004. Introduction to the finite element method, lecture notes [PowerPoint Presentation]. <https://homepages.cae.wisc.edu/~suresh/ME964Website/M964Notes/Notes/intro/em.pdf>.
- Nimmo, F., Giese, B., Pappalardo, R.T., 2004. What is the Young’s Modulus of ice? Accessed on July 18 2019. <https://www.lpi.usra.edu/meetings/europa2004/pdf/7005.pdf>.
- O’Brien, A., 2010. A Simple Introduction to Finite Element Analysis. Accessed on October 31 2019. <https://pdfs.semanticscholar.org/9253/71ec537d4fa8d8df154950626f570c8897e3.pdf>.
- O’Neill-Yates, C., 2018. Investigation shows Husky’s decision not to move out of iceberg’s path in close call “economically driven.” Canadian Broadcasting Corporation. Accessed on October 22 2019. <https://www.cbc.ca/news/canada/newfoundland-labrador/husky-iceberg-suspension-searose-fpso-suspension-cnlop-offshore-1.4551362>.

- Orheim, O., 1980. Physical characteristics and life expectancy of tabular Antarctic icebergs. *Annals of Glaciology* 1, 11–18.
<https://doi.org/10.3189/S0260305500016888>.
- Overland, J.E., Wang, M., 2013. When will the summer Arctic be nearly sea ice free? *Geophysical Research Letters* 40, 2097–2101. <https://doi.org/10.1002/grl.50316>.
- Patil, H., Jeyakarthykeyan, P.V., 2018. Mesh convergence study and estimation of discretization error of hub in clutch disc with integration of ANSYS, in: IOP Conference Series: Materials Science and Engineering. Presented at the 2nd International conference on Advances in Mechanical Engineering, Jaipur, India, 12 pp. <https://doi.org/10.1088/1757-899X/402/1/012065>.
- Petrovic, J., 2003. Review Mechanical properties of ice and snow. *Journal of Materials Science* 38, 1–6. <https://doi.org/10.1023/A:1021134128038>.
- Pizzolato, L., Howell, S.E.L., Derksen, C., Dawson, J., Copland, L., 2014. Changing sea ice conditions and marine transportation activity in Canadian Arctic waters between 1990 and 2012. *Climatic Change* 123, 161–173.
<https://doi.org/10.1007/s10584-013-1038-3>.
- Reddy, J.N., 2006. *An Introduction to the Finite Element Method*, 3rd ed. McGraw-Hill, New York, New York.
- Reeh, N., Thomsen, H.H., Higgins, A.K., Weidick, A., 2001. Sea ice and the stability of north and northeast Greenland floating glaciers. *Annals of Glaciology* 33, 474–480. <https://doi.org/10.3189/172756401781818554>.
- Rignot, E., Steffen, K., 2008. Channelized bottom melting and stability of floating ice shelves. *Geophysical Research Letters* 35, L02503.
<https://doi.org/10.1029/2007GL031765>.
- Rignot, E., Velicogna, I., van den Broeke, M.R., Monaghan, A., Lenaerts, J.T.M., 2011. Acceleration of the contribution of the Greenland and Antarctic ice sheets to sea level rise. *Geophysical Research Letters*. 38, 5 pp.
<https://doi.org/10.1029/2011GL046583>.
- Robe, R.Q., 1980. Iceberg drift and deterioration, in: *Dynamics of Snow and Ice Masses*. Academic Press, New York, 211–258.
- Roylance, D., 2001. Stress-strain curves. 15 pp. https://ocw.mit.edu/courses/materials-science-and-engineering/3-11-mechanics-of-materials-fall-1999/modules/MIT3_11F99_ss.pdf.

- Savage, S.B., 2001. Aspects of iceberg deterioration and drift, in: Balmforth, N.J., Provenzale, A. (Eds.), *Geomorphological Fluid Mechanics*. Springer, Berlin, 279–318. https://doi.org/10.1007/3-540-45670-8_12.
- Savvides, N., Bell, T.J., 1993. Hardness and elastic modulus of diamond and diamond-like carbon films. *Thin Solid Films* 228, 289–292. [https://doi.org/10.1016/0040-6090\(93\)90618-Y](https://doi.org/10.1016/0040-6090(93)90618-Y).
- Sazidy, M., 2020. *Ice Island Deterioration Model Technical Manual*. Water and Ice Research Laboratory, Department of Geography and Environmental Studies, Carleton University, Ottawa. <https://doi.org/10.22215/wirl/2020.1>.
- Sazidy, M., Crocker, G., Mueller, D., 2019. A 3D numerical model of ice island calving due to buoyancy-driven flexure. *Proceedings of the 25th International Conference on Port and Ocean Engineering under Arctic Conditions*. Presented at the Port and Ocean Engineering under Arctic Conditions, Delft, Netherlands. 12 pp. <http://www.poac.com/Papers/2019/pdf/POAC19-008.pdf>.
- Scambos, T., Sergienko, O., Sargent, A., MacAyeal, D., Fastook, J., 2005. ICESat profiles of tabular iceberg margins and iceberg breakup at low latitudes. *Geophysical Research Letters* 32, 4 pp. <https://doi.org/10.1029/2005GL023802>.
- Schulson, E. M. 1999. The structure and mechanical behavior of ice. *JOM* 51(2), 21-27. doi:10.1007/s11837-999-0206-4.
- Skotny, Ł., 2019. What are Nodes and Elements in Finite Element Analysis? [WWW Document]. Enterfea. <https://enterfea.com/what-are-nodes-and-elements-in-finite-element-analysis>.
- Smith, L.C., Stephenson, S.R., 2013. New Trans-Arctic shipping routes navigable by midcentury. *Proceedings of the National Academy of Sciences* 110, E1191–E1195. <https://doi.org/10.1073/pnas.1214212110>.
- Snyder, S.A., Schulson, E.M., Renshaw, C.E., 2016. Effects of prestrain on the ductile-to-brittle transition of ice. *Acta Materialia* 108, 110–127. <https://doi.org/10.1016/j.actamat.2016.01.062>.
- Stern, A.A., Adcroft, A., Sergienko, O., Marques, G., 2017. Modeling tabular icebergs submerged in the ocean. *Journal of Advances in Modelling Earth Systems* 9, 1948–1972. <https://doi.org/10.1002/2017MS001002>.
- Stroeve, J., Serreze, M., Drobot, S., Gearheard, S., Holland, M., Maslanik, J., Meier, W., Scambos, T., 2008. Arctic sea ice extent plummets in 2007. *Eos, Transactions, American Geophysical Union* 89, 13–14. <https://doi.org/10.1029/2008EO020001>.

- Tournadre, J., Bouhier, N., Girard-Ardhuin, F., Rémy, F., 2015. Large icebergs characteristics from altimeter waveforms analysis. *Journal of Geophysical Research: Oceans* 120, 1954–1974. <https://doi.org/10.1002/2014JC010502>.
- Trevers, M., Payne, A.J., Cornford, S.L., Moon, T., 2019. Buoyant forces promote tidewater glacier iceberg calving through large basal stress concentrations. *The Cryosphere* 13, 1877–1887. <https://doi.org/10.5194/tc-13-1877-2019>.
- Unosson, M., 2005. On failure modelling in finite element analysis: material imperfections and element erosion (Doctoral Thesis). Linköpings Universitet, Linköping.
- Van Wychen, W., Copland, L., 2017. Ice island drift mechanisms in the Canadian high Arctic, in: Copland, L., Derek Mueller (Eds.), *Arctic Ice Shelves and Ice Islands*. Springer, Dordrecht, Netherlands, 287–316.
- Vasil'chuk, Y.K., 2015. Physical properties of glacial and ground ice, in: Khublaryan, M.G. (Ed.), *Types and Properties of Water*. United Nations Educational, Scientific and Cultural Organization, Moscow, Russia, 237–264.
- Vaughan, D.G., 1995. Tidal flexure at ice shelf margins. *Journal of Geophysical Research* 100, 6213–6224. <https://doi.org/10.1029/94JB02467>.
- Voitkovskii, K., 1962. The elastic properties of ice, in: *The Mechanical Properties of Ice*. Mekhanicheskii svoistva l'da, Moscow, Izd. Akademii Nauk SSSR, 1960, 99 pp.
- Wagner, T.J.W., Dell, R.W., Eisenman, I., 2017. An analytical model of iceberg drift. *Journal of Physical Oceanography* 47, 1605–1616. <https://doi.org/10.1175/JPO-D-16-0262.1>.
- Wagner, T.J.W., James, T.D., Murray, T., Vella, D., 2016. On the role of buoyant flexure in glacier calving. *Geophysical Research Letters* 43, 232–241. <https://doi.org/10.1002/2015GL067247>.
- Wagner, T.J.W., Wadhams, P., Bates, R., Elosegui, P., Stern, A., Vella, D., Abrahamsen, E.P., Crawford, A., Nicholls, K.W., 2014. The “footloose” mechanism: Iceberg decay from hydrostatic stresses. *Geophysical Research Letters* 41, 5522–5529. <https://doi.org/10.1002/2014GL060832>.
- Wang, E., Nelson, T., Rauch, R., 2004. Back to elements - tetrahedra vs. hexahedra. CAD-FEM GmbH. Munich, Germany. Accessed on June 28 2019. <https://support.ansys.com/staticassets/ANSYS/staticassets/resourcelibrary/confpaper/2004-Int-ANSYS-Conf-9.PDF>.

Zuur, A.F., Ieno, E.N., Elphick, C.S., 2010. A protocol for data exploration to avoid common statistical problems: Data exploration. *Methods in Ecology and Evolution* 1, 3–14. <https://doi.org/10.1111/j.2041-210X.2009.00001.x>.

8.0 Appendix A

8.1 Simulation video of an ice island mesh 1 – uniform

See here for the supplementary file (<https://doi.org/10.22215/etd/2020-m011701.1>).

The perspective of this simulation video is from the bottom surface of the ice island and shows the highest stresses (yellow-red colour) concentrating towards the centre of the ice island. Three large fractures radiate outwards from this area towards the end of the video, which were not thought to be reasonable based on the results of the corresponding ice island calving plot. **Figure 8.1** shows the calving plot, along with stills of the simulation from different perspectives.

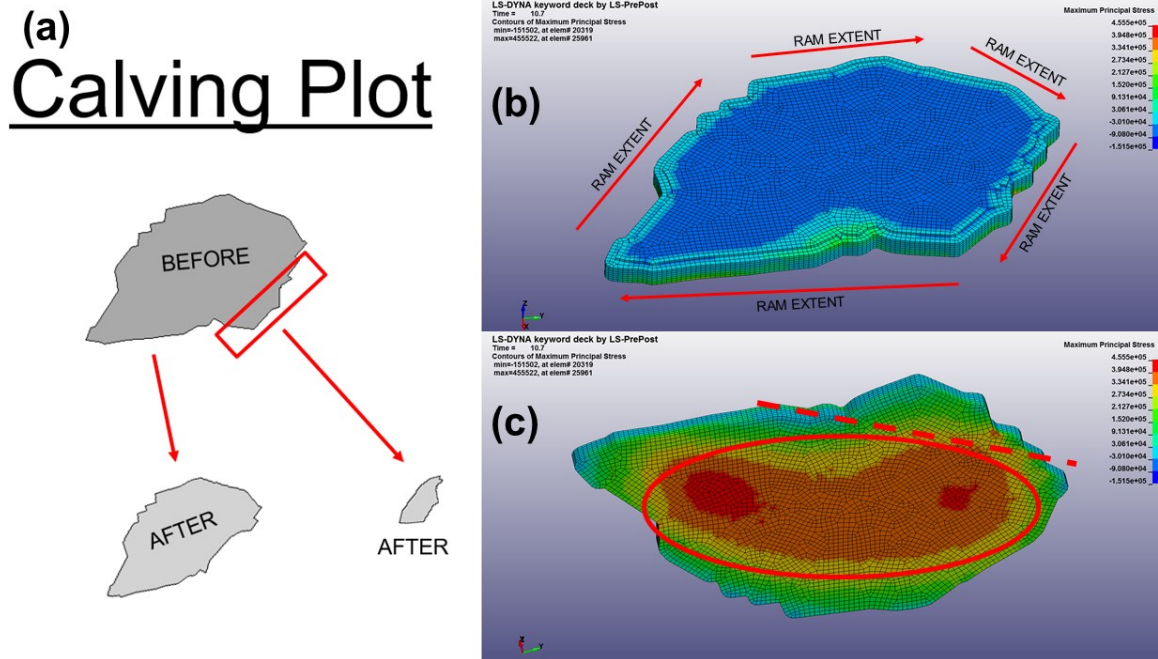


Figure 8.1: A calving plot and the simulation results from an ice island (“20110705_214859_r1_0_BSS_20”) with a 40 m long uniform ram. (a) shows the polygon before calving occurred and the fragments it produced after the event. **(b)** shows the surface of the ice island mesh and the uniform extent of the 40 m long ram. **(c)** shows the highest stresses concentrating towards the centre of the ice island bottom surface (red circle). The red dotted line indicates where calving is inferred to occur based on the calving plot.

9.0 Appendix B

9.1 Simulation video of an ice island mesh 2 – localized

See here for the supplementary file (<https://doi.org/10.22215/etd/2020-m011701.2>).

The perspective of this simulation video is from the bottom surface of the ice island and shows the highest stresses (yellow-red colour) concentrating towards the edge adjoined by the ram (not visible from this perspective). A fracture propagates along this edge towards the end of the video, which was thought to be reasonable based on the results of the corresponding ice island calving plot. **Figure 9.1** shows the calving plot, along with stills of the simulation from different perspectives.

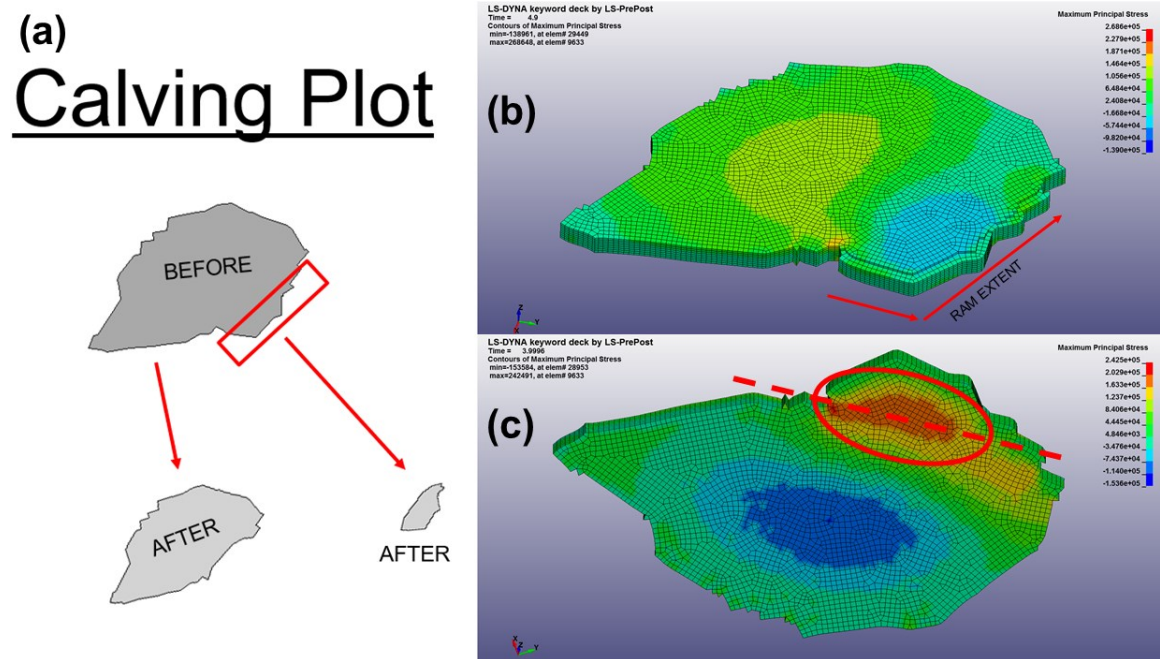


Figure 9.1: A calving plot and the simulation results from an ice island (“20110705214859_r1_0_BSS”) with a 40 m long localized ram. (a) shows the polygon before calving occurred and the fragments it produced after the event. (b) shows the surface of the ice island mesh and the localized extent of the 40 m long ram. (c) shows highest stresses concentrating towards an edge of the ice island bottom surface (red circle). The red dotted line indicates where calving is inferred to occur based on the calving plot.

10.0 Appendix C

10.1 Simulation video of an ice island mesh 3 – localized, shortened

See here for the supplementary file (<https://doi.org/10.22215/etd/2020-m011701.3>).

The perspective of this simulation video is from the bottom surface of the ice island and shows the highest stresses (yellow-red colour) concentrating towards the edge adjoined by the ram (not visible from this perspective), despite having a shortened ram. A similar fracture to the one indicated in Appendix B propagates towards the end of the simulation.

Figure 10.1 shows the calving plot, along with stills of the simulation from different perspectives.

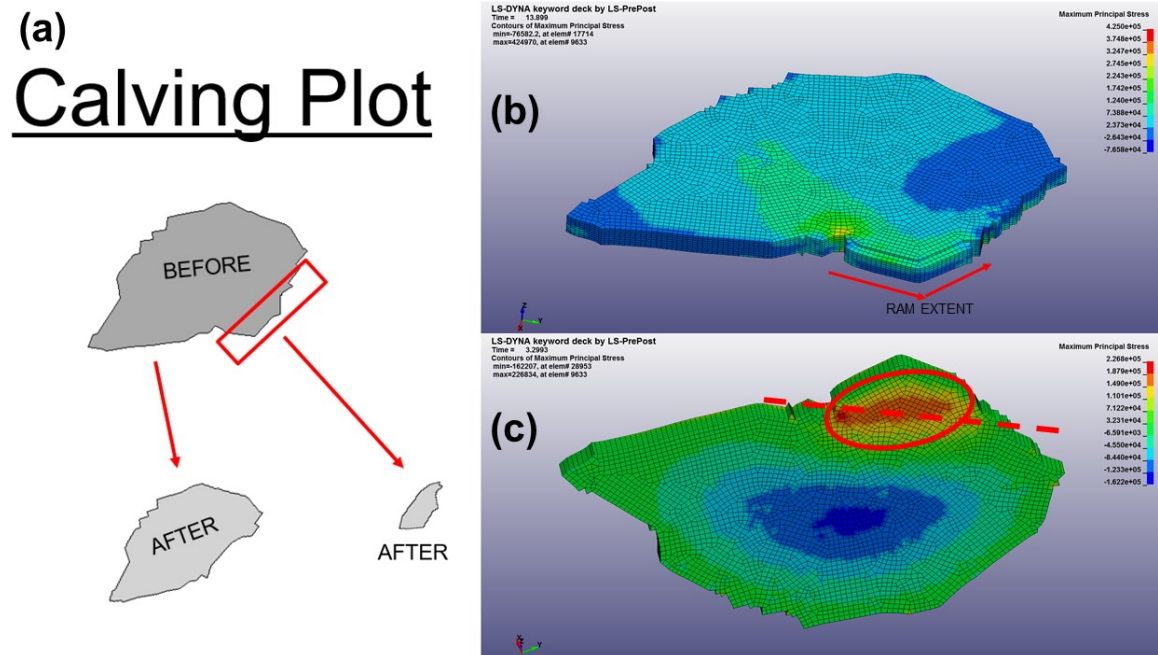


Figure 10.1: A calving plot and the simulation results from an ice island (“20110705_214859_r1_0_BSS”) with a 40 m long localized ram with its extent reduced by half. (a) shows the polygon before calving occurred and the fragments it produced after the event. (b) shows the surface of the ice island mesh and the localized extent of the 40 m long ram (reduced). (c) shows high stresses concentrating towards an edge of the ice island bottom surface (red circle). The red dotted line indicates where calving is inferred to occur based on the calving plot.